TU Delft

Delft University of Technology

Document Version
Final published version

Licence
CC BY

Citation (APA)
Jansari, C., Ybarra, D. C., Langelaar, M., Ayas, C., & Masania, K. (2026). Design for tape-reinforced additive manufacturing using geometric projection topology optimization. *Additive Manufacturing* , *127*, Article 105320. https://doi.org/10.1016/j.addma.2026.105320

Important note
To cite this publication, please use the final published version (if applicable).
Please check the document version above.

Copyright
In case the licence states “Dutch Copyright Act (Article 25fa)”, this publication was made available Green Open Access via the TU Delft Institutional Repository pursuant to Dutch Copyright Act (Article 25fa, the Taverne amendment). This provision does not affect copyright ownership.
Unless copyright is transferred by contract or statute, it remains with the copyright holder.

Sharing and reuse
Other than for strictly personal use, it is not permitted to download, forward or distribute the text or part of it, without the consent of the author(s) and/or copyright holder(s), unless the work is under an open content license such as Creative Commons.

Takedown policy
Please contact us and provide details if you believe this document breaches copyrights.
We will remove access to the work immediately and investigate your claim.

This work is downloaded from Delft University of Technology.

Additive Manufacturing 127 (2026) 105320

Contents lists available at ScienceDirect

Additive Manufacturing

journal homepage: www.elsevier.com/locate/addma

Research paper

Design for tape-reinforced additive manufacturing using geometric projection topology optimization

Chintan Jansari [a], David Canosa Ybarra [a], Matthijs Langelaar [b], Can Ayas [b], Kunal Masania [a,*]

[a] Shaping Matter Lab, Faculty of Aerospace Engineering, Delft University of Technology, Delft, 2629 HS, The Netherlands
[b] Faculty of Mechanical Engineering, Delft University of Technology, Delft, 2628 CD, The Netherlands

ARTICLE INFO

Keywords:
Topology optimization
Additive manufacturing
Automated tape laying
Fiber-reinforced composites
Sustainability

ABSTRACT

The pursuit of high-performance structures requires innovative manufacturing approaches that balance multiple competing factors. This work focuses on one such novel approach, named Advanced Tape Laying Additive Manufacturing (ATLAM), that integrates the characteristics of automated tape laying and additive manufacturing. ATLAM supported by a dedicated complementary design tool can provide a unique ability to balance mechanical performance, manufacturing flexibility, and eco-efficiency. To exploit the full potential of ATLAM in manufacturing lightweight sustainable structures, we aim to develop, verify and experimentally validate a computational design tool rooted in topology optimization. We use geometric projection topology optimization framework, and tailor it to accommodate ATLAM's unique features and constraints. We customize the geometric primitive, the projection & material interpolation schemes and design/manufacturing constraints. Then, based on numerical investigation, we showcase excellent effectiveness and robustness of the proposed approach in optimizing geometry and reinforcement placements and designing stiffer yet manufacturable structures. An environmental impact constraint is incorporated to enable a design choice on sustainability. Finally, we experimentally validate our proposed approach, paving the way for reliable use in real-world applications.

1. Introduction

Fiber-Reinforced Composites (FRCs) [1] are widely used for structural applications such as aerospace [2,3], automotive [4,5], and civil-infrastructure [6,7] industries, where lightweight, stiffness and fatigue tolerance are important. Traditionally, these FRC structures were manufactured as laminates by stacking several plies with uniform fiber orientations. Despite their high specific stiffness and strength, these laminates with uniform fiber orientations were able to harness only a limited portion of the much greater potential offered by spatially varying fiber orientations. This long-standing limitation was later addressed by the advent of advanced fiber placement techniques, such as filament winding, automated fiber placement, and automated tape laying [8]. Advanced fiber placement techniques could lay fibers with spatially varying orientations, a capability that provided superior mechanical performance for FRCs in stress distribution, buckling, and stiffness. In addition, a transition from thermoset-based to thermoplastic-based composites enabled fusion-bonding by applying in situ heat and pressure without the need for a separate curing step, as in thermoset-based composites. Together, automated fiber placement techniques with the adoption of thermoplastic-based composites have fueled the renewed use of FRCs in various industries [9].

Overcoming barriers to the adoption of FRCs in the industry requires a balance between multiple competing factors, such as strength and weight, precision and speed, cost and quality, material use and sustainability, or complexity and manufacturability. Therefore, next to an innovative manufacturing process that can adaptively and strategically balance such crucial yet competing factors, a smart design workflow that can exploit the full potential of such processes could prove vital. Here, we focus in particular on one such novel FRC manufacturing process, called advanced tape laying additive manufacturing, and a novel process tailored design optimization workflow.

1.1. Advanced tape laying additive manufacturing

Fig. 1a presents the concept of advanced tape laying additive manufacturing. This is a hybrid approach merging two well-known manufacturing processes - automated tape laying and additive manufacturing.

* Corresponding author.
E-mail address: K.Masania@tudelft.nl (K. Masania).

https://doi.org/10.1016/j.addma.2026.105320
Received 10 February 2026; Received in revised form 8 July 2026; Accepted 28 July 2026
Available online 3 August 2026
2214-8604/© 2026 The Authors. Published by Elsevier B.V. This is an open access article under the CC BY license (http://creativecommons.org/licenses/by/4.0/).

Automated Tape Laying (ATL) is an advanced FRC manufacturing technique that uses automated equipment to lay continuous pre-impregnated fiber tapes to produce high-quality FRCs [9]. ATL is similar to Automated Fiber Placement (AFP), but ATL is suitable for wider tape materials and larger structures. In the ATL process, the layers of unidirectional tape are progressively laid on a mandrel. The surfaces of the new and previous tape layers are heated near the contact point using a heat source, before pressing to fuse them together. A typical in-situ consolidation ATL process is shown in Fig. 1a. With these steps, the ATL process is capable of producing strong lightweight industrial structures. However, the tapes' geometric inflexibility, caused by the stiffness of the carbon fiber, limits the shaping freedom in manufacturing. As a result, ATL-manufactured structures are usually flat or with mild curvatures. In addition, they often have a considerable CO_2-footprint due to the extensive use of carbon fibers. Hence, a larger CO_2-footprint and limited shaping freedom limit the scope of ATL in the manufacturing of sustainable and geometrically complex FRCs.

Additive Manufacturing (AM) [10–12] exhibits extraordinary form freedom contrary to ATL. AM can manufacture much more complex geometric structures that are also eco-efficient (lower embodied CO_2) compared to ATL-manufactured FRCs. That being said, AM is not free from limitations. AM-manufactured polymer structures have lower specific strength and stiffness compared to FRCs. Therefore, the concept of AM has also been extended for FRC manufacturing, particularly through extrusion-based AM [13] In short-fiber AM, fiber pellets are fed into the nozzle where they tend to align in the direction of melt flow [13–15]; while in Continuous-Fiber AM (CFAM), dry fibers or prepreg fibers are fed through a separate nozzle or co-extruded with the polymer matrix during the printing process [16,17] The discontinuous fibers in short-fiber structures often lead to inferior mechanical performance to those manufactured using CFAM. CFAM enables controlled fiber placement. However, the mechanical properties of CFAM-manufactured structures still cannot match those of conventionally manufactured counterparts. This is mainly due to higher void density, inadequate filament bonding, and limited fiber impregnation [18,19]. Additionally, achieving a fiber volume fraction greater than 50% in AM-manufactured FRCs remains a critical challenge [20]. The AM process is also slower and thus more costly, embodies uncertainties and lacks standardized design rules. This process speed and cost of AM remain major obstacles to the large-scale adoption of AM in industry.

We highlight that ATL and AM show a number of complementary characteristics, especially in strength, manufacturing flexibility, and eco-efficiency, worthy to integrate into a single process. In Advanced Tape Laying Additive Manufacturing (ATLAM), first a bead of polymer substrate material is printed additively. Then, on top of the printed bead, a heated tape is laid and compressed. These steps are repeated to construct an entire structure as shown in Fig. 1a. We have presented an ATLAM setup developed by CEAD B.V. [21] in Figure S1 [22]. The primary advantage of ATLAM, that combines characteristics of ATL and AM, is that it allows a smart trade-off among strength, manufacturing flexibility, and eco-efficiency according to desired requirements. In addition, ATLAM is expected to achieve manufacturing times comparable to or slightly faster than conventional layer-by-layer AM, particularly when considering time per unit stiffness achieved through tape reinforcement.

Given the versatility of the ATLAM process, a design workflow tailored to ATLAM to unlock its full potential is essential. This requires a due account to limitations of manufacturing process. The alignment between design and manufacturing allows us to create products that are not only functional and reliable but also practical to produce and avoids costly redesigns. This concept of designing for a given manufacturing process is called 'design-for-manufacturing' [23–26]. In this paper, we propose 'design for tape-reinforced additive manufacturing' or 'design for ATLAM', by utilizing a computational design method called topology optimization. Topology optimization optimizes the geometric layout of the structure for a desired design target such as material efficiency. For ATLAM, topology optimization can be utilized to optimize both topology and reinforcement placement, significantly improving the strength-to-weight ratio and producing lightweight FRCs as shown in Fig. 1b.

1.2. Topology optimization

Topology Optimization (TO) is a computational design method that determines the best possible material layout within a given design domain for a mathematically defined objective and constraints [27]. In simple engineering terms, TO iteratively removes, adds, and redistributes the material of the structure to improve its performance. TO has several variants based on the manner in which the design are represented. Typically, TO is referred to implicit-design description as in density-based TOs [28] (which use a pseudo-density field as the design representation) or level-set TOs [29] (which use a higher dimensional level-set function as the design representation).

In the past decade, a new set of TO approaches has emerged called Feature-mapping TOs [30,31]. Feature-mapping TOs encompasses methods such as, feature-based TO [32], smooth boundary TO [33], circular-shaped mask TO [34], Moving Morphable Component (MMCs) TO [35], Geometric-projection TO [36], Moving Morphable Void (MMV) TO [37], Moving Morphable Bars (MMBs) TO [38] and others. Feature-mapping TOs exploit a high-level parametric description, where the design is defined by a specific configuration of a set of explicit geometric features/primitives. The size, position, orientation, and arrangement of these primitives are modified to update the design. The explicit geometric parameters of all the primitives are utilized as the design variables, contrary to elemental densities, as in density-based TOs, or nodal values of the level-set function, as in level-set TOs. Compared to density-based TOs and level-set TOs, feature-mapping TOs are advantageous for better controlling the size and shape of geometric features in the design. For that reasons, our goal is to utilize a feature-mapping TO, so that the rectangular shape of the tape in the ATLAM process can be maintained and that the manufacturing constraints related to tape laying can be included in the optimization framework.

To design FRCs, TO are extended to optimize multiple other attributes in addition to topology such as fiber orientations, material volume fractions, stacking sequence, and thickness to leverage the benefits of variable stiffness [39]. These TO approaches differ in the optimization method employed, the optimization strategy (sequential or concurrent), the parameterization scheme, the structural scale, and the manufacturing constraints considered. Optimizing for multiple attributes provides a larger design space, but also incurs higher computational cost. Therefore, more frequently, only the fiber orientations are incorporated as an additional attribute.

The potential of simultaneously optimizing material distribution and fiber orientations was initially presented by Stegmann and Lund [40], Setoodeh et al. [41], and Nomura et al. [42]. Later, TO for FRCs demonstrated significant improvements in stiffness [43], stress concentration [44], buckling [45], and natural frequency [46]. More recently, Li et al. [47] and Xu et al. [48] integrated TO with continuous fiber paths by embedding manufacturable trajectories directly into structural layouts. Jung et al. [49] extended this concept to multiscale design through concurrent optimization of macroscale topology and microscale fiber size and orientation. For additive manufacturing, Almeida Jr. et al. [50] and Huang et al. [51] proposed concurrent optimization of topology, fiber orientations, and fiber content for printed composites. Later, manufacturability considerations such as curvature and misalignment, together with buckling, strength, and uncertainty objectives, were incorporated into TO, resulting in more robust and practical designs [52–55]. Neural-network-based frameworks have also been explored to enable high-resolution, efficient, and manufacturing-aware FRC design [56,57]. Fernandes et al. [58] further provided experimental validation of topology-optimized continuous fiber-reinforced composites, demonstrating the practical effectiveness of TO-designed

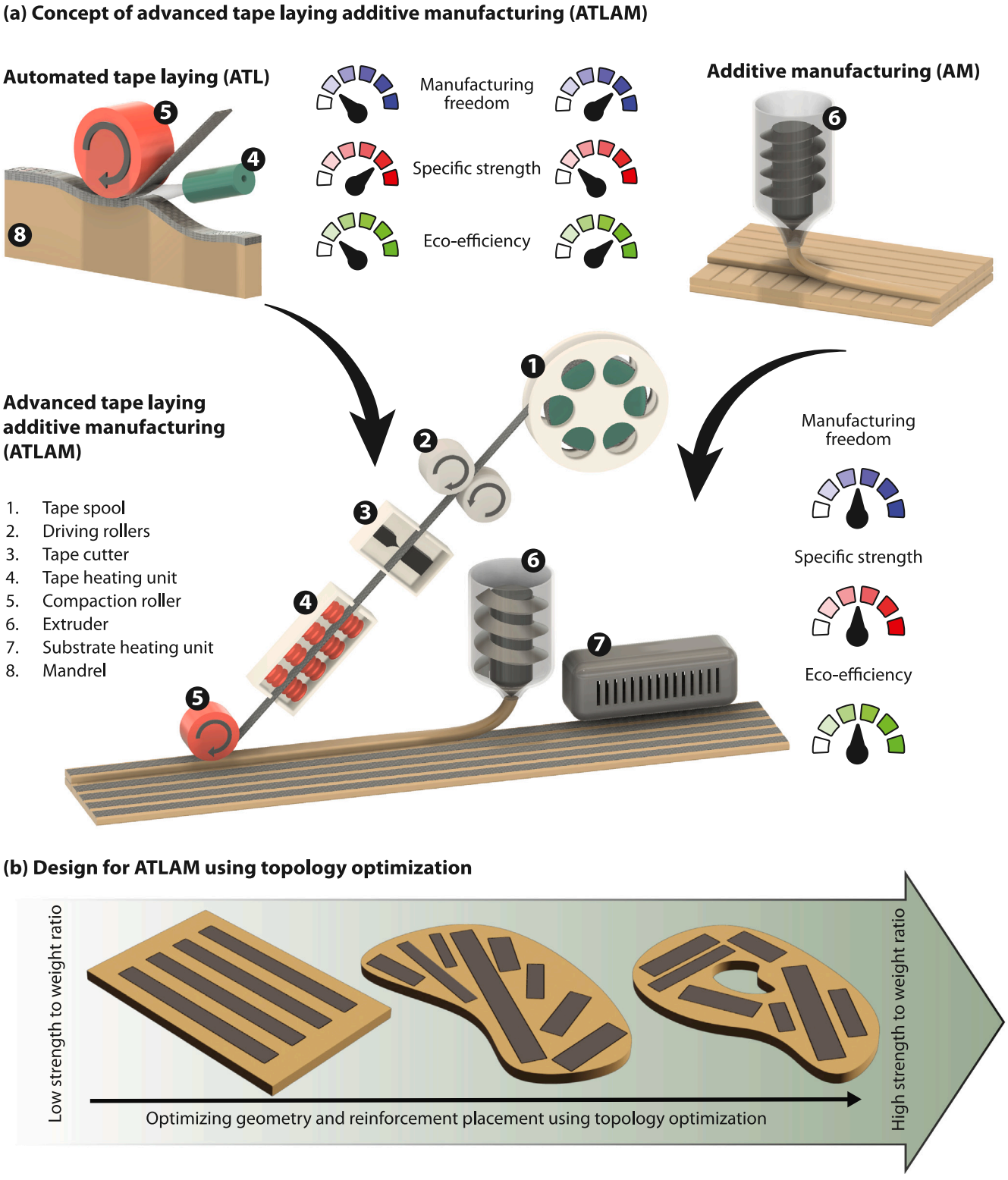


Fig. 1. (a) The concept of Advanced Tape Laying Additive Manufacturing (ATLAM), a combination of Automated Tape Laying (ATL) and Additive Manufacturing (AM). In ATLAM, tape reinforced composites are manufactured by laying and compressing heated tapes on top of the additively-laid substrate material. ATLAM provides trade-off among the advantages and limitations of ATL and AM, especially in specific strength, manufacturing freedom and eco-efficiency. (b) Design for ATLAM process using topology optimization. Both the part geometry, and reinforcement locations and orientations are optimized iteratively while ensuring the manufacturability for ATLAM. The optimization significantly increases the strength to weight ratio of the structures.

FRCs. Additional state-of-the-art developments of TO for FRCs are comprehensively discussed in the following review articles [25,39,59,60].

Some of the most relevant studies for our purpose are those that focus on optimizing multi-component systems or on multi-material feature-mapping TO. In multi-component systems, the topology and embedding of rigid objects (similar to tapes) are optimized simultaneously [38,61–66]. The embedded rigid objects for instance can represent the space reserved for assembly, bolts, rivets, or actuators. These studies use a level-set or a finite-circle description to represent rigid embedded objects in a standard TO framework. However, these rigid objects do not change in size, nor are they constrained to remain within the extent of the substrate or host material. Additionally, the constraints that prevent the overlap of these objects are strict, disallowing any overlap even during the intermediate iterations of the optimization. Under such strict constraint, the movement of each embedded object is restricted by the other surrounding objects. Consequently, exploring designs that require substantial movement of the objects becomes increasingly challenging. Hence, these constraints, to a certain degree, restrict the exploration scope of the optimization.

In the context of multi-material feature-mapping TO, Zhang et al. [67] used primitives made of different isotropic materials in MMC TO. Sun et al. [68] extended multi-material MMC TO for anisotropic FRCs. They employed an addition fiber angle variable per primitive. Later, based on their earlier work on MMB TO [38], Wang et al. developed a design framework for a multi-component system where two sets of primitives are used, one for the base material and another for the embedded objects. Hoang et al. [69] formulated a concentric multi-material primitive in the MMB framework, where the outer material represented the coating surrounding the base material. Almeida et al. exploited the incorporation of Geometric Project TO [70] with density TO to design smart structure with piezoelectric stack actuators. Gandhi et al. [71] employed GPTO to design variable-stiffness composite laminates manufacturable through a continuous fiber filament fabrication process. Larsen et al. [72] employed a skeleton-curve parameterization based on the absolute nodal coordinate formulation, enabling fiber orientations to align with the skeleton curve while also ensuring fiber continuity across multiple components.

Despite the research efforts described above, no TO framework for FRCs suitable for ATLAM process exists, particularly accounting for rectangular transversely isotropic tapes, the requirement for a supporting substrate embedding each tape, the selective nature of tape deposition and process-specific constraints such as prohibiting tape overlap, excessively short tapes, and straddling tape placements. These limitations highlight the need for a TO framework tailored for ATLAM that optimizes both geometry and reinforcement tape placement, while ensuring the manufacturability of the designed structures.

To bridge this research gap, we propose a novel ATLAM-tailored TO framework rooted in a feature-mapping TO, called Geometric Projection TO (GPTO) [36]. GPTO differs from other feature-mapping TOs by introducing an additional continuous variable $\in [0,1]$, for the disappearance and reappearance of a primitive in the design. The continuous size variable provides better convergence behavior to GPTO, especially with multiple constraints.

The main contributions of the current work are (1) the formulation of a novel GPTO framework tailored to ATLAM process, (2) verification of the proposed framework by solving several numerical examples, (3) presentation of the effectiveness of the framework in balancing characteristics such as stiffness and eco-efficiency of ATLAM, and (3) validation of the numerical results with experiments.

2. Topology optimization framework

GPTO was proposed by Norato and collaborators [36,73], and has subsequently been extended to FRC bars [74], plates [75] and laminates [76] within the single material formulation. Fig. 2a presents a flow chart of the standard GPTO formulation. As shown in the figure, the design is described first using geometric primitives, subsequently mapped into a pseudo-density field over a mesh before utilizing it to represent the material distribution for a finite element model, similar to a density-based topology optimization. To employ the GPTO framework for ATLAM, we need to customize several of its components, such as a specialized primitive that mimics the manufacturing process (Section 2.1), a specialized projection scheme to map the primitive description into pseudo-density fields (Section 2.3), a specialized material interpolation scheme that matches physics (Section 2.4), and finally, several specialized design and manufacturing constraints to ensure the manufacturability (Section 2.5).

2.1. Design description

We formulate a multi-material primitive that provides a high-level parametric geometric description for the structures manufactured by the ATLAM process. The primitive is formulated as two nested rectangles, the inner one representing the transversely isotropic tape, while the outer one represents the isotropic substrate. A primitive with both rectangles is shown in Fig. 2b.

The inner rectangle is described by the coordinates of the endpoints of the major mid-axis $(x_{t1}, y_{t1})\&(x_{t2}, y_{t2})$ and the width W_t. The outer rectangle is described with reference to the inner rectangle using two length variables $L_{1s}\&L_{2s}$ and the width W_s. Using these design variables, the outer rectangle can also be described in terms of the end points of the major mid-axis and width. The end points of the major mid-axis of outer rectangle, denoted as $(x_{s1}, y_{s1})\&(x_{s2}, y_{s2})$, can be written as,

$$(x_{s1}, y_{s1}) = (x_{t1}, y_{t1}) - L_{1s}\mathbf{n}, \tag{1a}$$

$$(x_{s2}, y_{s2}) = (x_{t2}, y_{t2}) + L_{1s}\mathbf{n}, \tag{1b}$$

where $\mathbf{n} = \mathbf{v}/\|\mathbf{v}\|$, with $\mathbf{v} = (x_{t2}, y_{t2}) - (x_{t1}, y_{t1})$, is the unit normal in the direction of the major mid-axis of the inner rectangle. Exploiting the same description, based on endpoint coordinates and width, for both rectangles helps to detail the projection scheme and the sensitivity analysis, described in subsequent sections.

In addition to geometric variables, the primitive has two so-called size variables, denoted as α_t, $\alpha_s \in [0,1]$, following nomenclature and notation introduced in [74]. The size variables allow removal and reintroduction of the tape and substrate in the design. The continuous nature and additional design dimensions of these size variables provide better optimization convergence. The value 0 indicates that the tape or substrate is not present in the design, while 1 means that it is present. To ensure a full black-and-white design, we need to ensure that all size variables converge to a 0 or 1 value at the end of optimization.

With the given description, a general primitive b can be described using a set of 10 design variables $\mathbf{z}^b = [x_{t1}^b, y_{t1}^b, x_{t2}^b, y_{t2}^b, W_t^b, \alpha_t^b, L_{s1}^b, L_{s2}^b, W_s^b, \alpha_s^b]$. Although we use this particular primitive description, the methodology is not restricted by the choice of parameterization. The other design descriptions and other suitable shapes are equally applicable in the framework.

2.2. Generalized compliance minimization problem

In this subsection, we formulate the GPTO problem. We consider that the structures are made of n_b primitives and can be described using $n_d = 10\, n_b$ design variables, $\mathbf{z} = \left[\mathbf{z}^1, \mathbf{z}^2, \ldots, \mathbf{z}^b, \ldots, \mathbf{z}^{n_b}\right]$ with $\mathbf{z}^b$ being a set of 10 design variables for b^{th}-primitive as defined earlier. We assume that the boundary conditions are design independent and that there are no applied body loads. With the above-mentioned assumptions, a compliance minimization problem can be written as,

$$\min_{\mathbf{z}\in\mathbb{R}^{n_d}} \; c(\mathbf{z}, \mathbf{U}) = \mathbf{U}^T\mathbf{K}\mathbf{U}, \tag{2a}$$

subject to,

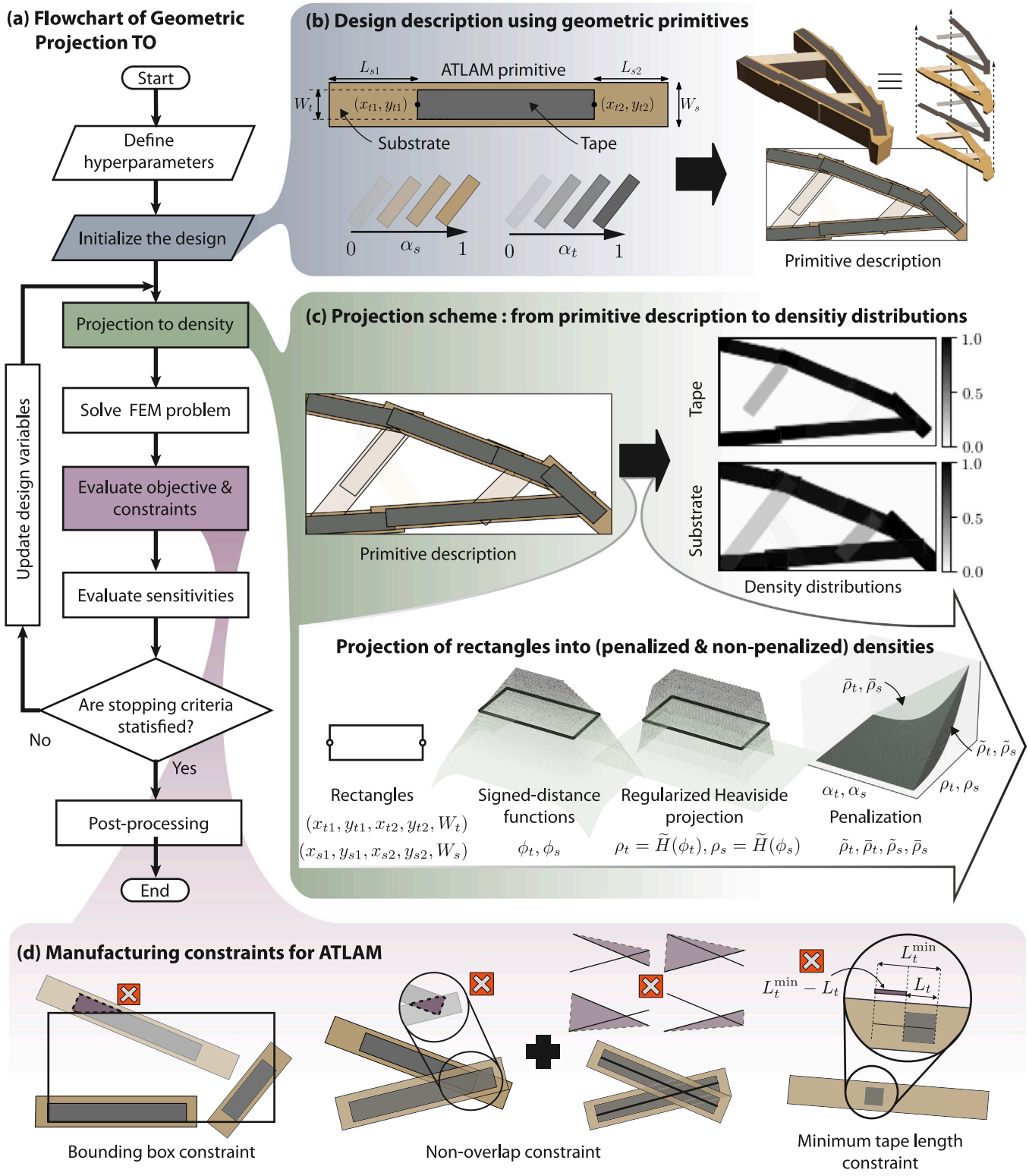


Fig. 2. A detailed description of the Geometric Projection Topology Optimization (GPTO) formulation for ATLAM. (a) A flowchart showcasing the key steps in the method. (b) The primitive description based on the proposed ATLAM primitive. The ATLAM primitive, consisting two nested rectangles, is described by 8 geometric parameters $(x_{t1}, y_{t1}, x_{t2}, y_{t2}, W_t, L_{s1}, L_{s2}, W_s)$ and two size (α_t, α_s) parameters. (b) A projection scheme that transforms the ATLAM- primitive description into tape densities $\bar{\rho}_t, \tilde{\rho}_t$ & substrate densities $\bar{\rho}_s, \tilde{\rho}_s$. (c) ATLAM-specific manufacturing constraints that are incorporated into the method: bounding box constraint (to prevent the tapes from straddling the boundary), non-overlap constraint (to prevent the overlapping of the tapes), and tape minimum length constraint (to prevent shorter tapes).

$$\boldsymbol{g}(\mathbf{z},\mathbf{U}) \le 0, \tag{2b}$$

$$z_i^{\min} \le z_i \le z_i^{\max}, \qquad \forall z_i \in \mathbf{z}, \quad i = 1,2,\dots,n_d, \tag{2c}$$

$$\mathbf{KU} = \mathbf{F}, \tag{2d}$$

where c is the compliance measure of the structure (2 × elastic strain energy); $\boldsymbol{g}$ is a set of generalized constraints (including a standard volume fraction constraint) to apply a design restriction or to ensure the manufacturability of the structures. $z_i^{\min}$ and $z_i^{\max}$ are the upper and lower limits of the i^{th}-design variable z_i; $\mathbf{K}$, $\mathbf{U}$ and $\mathbf{F}$ are the global stiffness matrix, the global displacement vector, and the global force vector, respectively. Please note that the state equation in Eq. (2d) is not applied as an explicit constraint in optimization; rather, $\mathbf{U}$ containing state variables is solved in each iteration after projecting the primitives to a density field on a mesh using the finite element method.

2.3. Density projection

As mentioned earlier, the basic idea of GPTO involves mapping the high-level parametric description into a pseudo-density field [36]. We project our high-level parametric description into two pseudo-density fields, one related to the tape phase and the other related to the substrate phase, as shown in Fig. 2c. This mapping has to be differentiable to ensure well-defined sensitivities.

First, we explain the projection scheme for a single material primitive. The projected density with respect to a primitive b, ρ^b at a point $\mathbf{x} = (x, y)$ is defined as [36],

$$\rho^b(\mathbf{x},\mathbf{z}^b,r) := \frac{|B_{\mathbf{x}}^r \cap \Omega^b(\mathbf{z}^b)|}{|B_{\mathbf{x}}^r|}, \tag{3}$$

where $B_{\mathbf{x}}^r$ is the ball domain of radius r centered at the point $\mathbf{x}$ and Ω^b is the primitive domain. For arbitrary shaped Ω^b, the calculation of the numerator is not straightforward. Therefore, under the assumption of r being sufficiently small and Ω^b being a smooth closed manifold, the intersection area is commonly approximated as an area of a circular segment of height $h = r - \phi^b$ in 2D [36], where $\phi^b(\mathbf{x},\mathbf{z}^b)$ is the signed distance function from $\mathbf{x}$ to the primitive domain boundary $\partial\Omega^b$. We consider the density to be piecewise continuous over the elements, with values evaluated at the center of the elements; and the size of the sample window r is fixed. Thus, the projected density associated with the e^{th}-element and the b^{th}-primitive is written as,

$$\rho^{b,e}(\mathbf{z}^b) := \begin{cases} 0, & \text{if } \phi^b/r < -1, \\ \widetilde{H}(\phi^{b,e}/r), & \text{if } -1 \le \phi^b/r \le 1, \\ 1, & \text{if } \phi^b/r > 1, \end{cases} \tag{4}$$

where $\widetilde{H}$ is the regularized Heaviside function written as,

$$\widetilde{H}(x) = 1 + \frac{x\sqrt{1-x^2} - \arccos x}{\pi}. \tag{5}$$

Similarly, for our work, the inner and outer rectangles of each primitive are projected as shown in Fig. 2c. The signed distance functions for both rectangles are defined using the rectangular signed distance function given in [70]. Then, the signed distance functions are individually assigned to their corresponding densities, $\rho_t^{b,e}$ and $\rho_s^{b,e}$, with t and s representing the tape and substrate, respectively, as,

$$\rho_t^{b,e} = \widetilde{H}(\phi_t^{b,e}), \quad \text{and} \quad \rho_s^{b,e} = \widetilde{H}(\phi_s^{b,e}). \tag{6}$$

To introduce the effect of size variables in the analysis, the densities are multiplied by their respective size variables. The new modified densities $\bar{\rho}_t^{b,e}$ and $\bar{\rho}_s^{b,e}$ are given as,

$$\bar{\rho}_t^{b,e} = \alpha_t^b \rho_t^{b,e}, \quad \text{and} \quad \bar{\rho}_s^{b,e} = \alpha_s^b \rho_s^{b,e}. \tag{7}$$

As discussed in Section 2.1, we need to ensure convergence of α_t^b and α_s^b to 0/1. To push the values of the size variables toward 0/1 as the optimization progresses, a numerical penalization scheme similar to the Solid Isotropic Material Interpolation (SIMP) scheme of density-based topology optimization is used. Hence, the penalized densities $\tilde{\rho}_t^{b,e}$ and $\tilde{\rho}_t^{b,e}$ can be written as,

$$\tilde{\rho}_t^{b,e} = (\alpha_t^b \rho_t^{b,e})^p, \quad \text{and} \quad \tilde{\rho}_s^{b,e} = (\alpha_s^b \rho_s^{b,e})^p, \tag{8}$$

where p is the penalization factor. Henceforth, with reference to penalized densities, $\bar{\rho}_t^{b,e}$ and $\bar{\rho}_s^{b,e}$ will be referred to as non-penalized densities.

Penalized densities are used for the compliance calculation via a material interpolation scheme, while non-penalized densities are used to calculate in the volume fraction constraint. Similarly to the SIMP concept, the difference between two interpolation schemes for size parameters will push their values toward 0/1.

2.4. Material interpolation scheme

Next, we formulate the material interpolation scheme that connects the density distributions to the physics of the problem. Considering a perfect bond between the tape surface and the corresponding substrate surface, both surfaces will deform with equal strain, so, we take the Voigt rule of mixtures to find the aggregate material matrix that assumes a uniform strain along the thickness direction. The elemental material matrix $\mathbb{C}^e$ is defined as,

$$\mathbb{C}^e = \mathbb{C}_{\text{void}} + \sum_{b=1}^{n_b} \left(h\ \tilde{w}_s^{b,e} \tilde{\rho}_s^{b,e} \left(\mathbb{C}_s^b - \mathbb{C}_{\text{void}}\right) + h_t \tilde{w}_{st}^{b,e} \tilde{\rho}_{st}^{b,e} \left(\mathbb{C}_t^b - \mathbb{C}_s^b\right) \right), \tag{9}$$

where $\tilde{\rho}_{st}^{b,e} = \tilde{\rho}_s^{b,e}\ \tilde{\rho}_t^{b,e}$; $\mathbb{C}_s^b$ and $\mathbb{C}_t^b$ are the elasticity matrix of the substrate and tape materials associated with b^{th}-primitive, respectively; $\mathbb{C}_{\text{void}}$ is the isotropic elasticity matrix of an extremely soft fictitious material associated to the void phase. The thickness of the entire structure is h and h_t is the total thickness of the tape reinforcement (h_t= tape thickness × number of tape layers). Here, the weight factors $\tilde{w}_s^{b,e}$ and $\tilde{w}_{st}^{b,e}$ are associated with the densities $\tilde{\rho}_s^{b,e}$ and $\tilde{\rho}_{st}^{b,e}$, respectively. These weight factors are in place to handle the overlap of primitives in a way similar to that in [74]. The weight factors define the fractional contribution associated with each primitive in regions where multiple primitives overlap. In our case, the overlap of transversely isotropic tapes is ultimately restricted by a constraint (which will be introduced in Section 2.5.3), whereas the substrate material is isotropic. Therefore, we use normalized density values as weight factors instead of the softmax arg function (as in [74]) to avoid additional nonlinearity. The weight factors are defined as,

$$w^{b,e} = \frac{\rho^{b,e}}{\sum_{b=1}^{n_b} \rho^{b,e}}. \tag{10}$$

2.5. Constraint functions

In this section, we formulate several design and manufacturing constraints for the optimization problem.

2.5.1. Volume fraction constraint

First, we apply a standard volume fraction constraint. The constraint is defined as,

$$g_v := \frac{V}{V_0} - f \le 0, \tag{11}$$

where f is the maximum allowed volume fraction; V_0 is the total volume of the design domain; and V is the volume of the structure calculated as,

$$V = \sum_{e=1}^{n_e} \sum_{b=1}^{n_b} \bar{w}_s^{b,e} \tilde{\rho}_s^{b,e} v_e, \tag{12}$$

with v_e being the volume of the e^{th}-element.

2.5.2. Bounding box constraint

The purpose of the bounding box constraint is to avoid the straddling positioning of the tapes with respect to the design domain boundaries (see Fig. 2d). This constraint is crucial from the manufacturing perspective, as cutting tapes in the finishing stage is rather cumbersome and often significantly worsens the manufacturing quality of final structure. We apply this constraint using the difference between the total tape volume calculated from the projected density, V_t, and from using design variables, ${}^{z}V_t$. The idea of the constraint is similar to that presented in [63] to prevent movable embedded holes from leaving the domain. The bounding box constraint is defined as,

$$g_b := \frac{{}^{z}V_t - V_t}{fV_0} \leq 0, \tag{13}$$

with

$$V_t = \sum_{e=1}^{n_e}\sum_{b=1}^{n_b} \rho_t^{b,e} v_e, \quad \text{and} \quad {}^{z}V_t = \sum_{b=1}^{n_b} {}^{z}V_t^b, \tag{14}$$

where ${}^{z}V_t^b = W_t^b L_t^b$, with $L_t^b = \|(x_{t1}^b, y_{t1}^b) - (x_{t2}^b, y_{t2}^b)\|$, is the tape volume of the b^{th}-primitive calculated directly from the design variables.

2.5.3. Non-overlap constraint

The non-overlap constraint ensures that the tapes do not overlap as shown in Fig. 2d. This constraint is due to a limitation of the ATLAM process, as laying a tape over tape creates a bulge in the current state-of-the-art of ATLAM process. However, this is not an issue for the substrate material. The elasticity matrix of the overlap regions for substrate material will behave same as the single isotropic material with the defined material interpolation scheme. In this constraint, we constrain the tape-overlapping design freedom by applying the non-overlap constraint.

Both non-overlap and bounding-box constraints have been utilized in the feature-mapping TO literature as forms of separation constraints. Common formulations include methods based on finite-circles, comparisons between implicit and explicit volume calculations, distances from the structural skeleton, and pseudo-density fields [30]. Frequently, these two functions are combined into a single unified constraint. Here, we utilize the non-overlap constraint similar to one proposed in [77]. The overlap constraint is formulated as the summation of two terms as,

$$g_o := \left(\frac{1}{fV_0}\sum_{e=1}^{n_e} \widetilde{R}\left(\sum_{b=1}^{n_b} \tilde{\rho}_{st}^{b,e} - 1\right) v_e + \beta_o\right) \leq 0, \tag{15}$$

where $\widetilde{R}$ is the smooth ramp function, defined as $\widetilde{R}(x) = (x + \sqrt{x^2 + \epsilon})/2$ with ϵ being a small positive number. The first term ensures the elemental tape volume does not exceed the volume of the element. However, this term alone is insufficient to resolve the overlap when two tapes, present in the design with $\alpha_t \approx 1$, completely intersect, as shown in Fig. 2d. In this scenario, the first term becomes insensitive to translation or shortening of the tape because the overlapping region remains the same. The optimizer therefore has no gradient information about design changes that could resolve the overlap configuration. So, to steer the design out of this situation, we add an extra term β_o penalizing the complete intersections of two primitives in a way that provides gradient information on how to resolve the intersection.

β_o is defined based on a quadrilateral formed by a pair of intersecting mid-axes. Each mid-axis divides the quadrilateral into two triangles as shown in Fig. 2d. We calculate the area of all four triangles and consequently, define the term β_o as,

$$\beta_o = \frac{1}{CV_0}\sum_{k}^{n_k} \min({}^{k}V^{11}, {}^{k}V^{12}, {}^{k}V^{21}, {}^{k}V^{22}), \tag{16}$$

where $n_k = n_b(n_b - 1)/2$ is the total number of pairs of mid-axes; C is a constant for normalization (In this work, $C = 0.01$); and ${}^{k}V^{ij}$ is the area of the j^{th}-triangle created by the i^{th}-diagonal (mid-axis) of the k^{th}-pair. It is given as,

$${}^{k}V^{ij} = \frac{1}{2}\alpha_s^a \alpha_t^a |(x_{t1}^b - x_{t2}^b)(y_{tj}^a - y_{t2}^b) - (x_{tj}^a - x_{t2}^b)(y_{t1}^b - y_{t2}^b)|, \tag{17}$$

with a and b are the global primitive numbers of i^{th}- and j^{th}- primitives of the k^{th}-pair, respectively.

2.5.4. Size variable penalization constraint

During the initial numerical experiments, we observed several cases where some of the size variables are stuck at intermediate values and do not converge to 0/1 as shown in Figure S1a. Although this solution is a local minimum, it does not represent a feasible design. This issue stems from the fact that the effect of the size variable on volume and stiffness becomes significantly larger if the associated primitive is long. Therefore, the size parameter cannot reach the 0/1 value without violating the volume fraction constraint or substantially compromising the stiffness.

To overcome this issue, we penalize the intermediate values of the size variables using an additional constraint called the size variable penalization constraint defined as,

$$g_\alpha := \frac{1}{fV_0}\sum_{b=1}^{n_b} \left(\alpha_s^b(1 - \alpha_s^b)\, {}^{z}V_s^b + \alpha_t^b(1 - \alpha_t^b)\, {}^{z}V_t^b\right) \leq 0, \tag{18}$$

where ${}^{z}V_s^b$ and ${}^{z}V_t^b$ are, respectively, the substrate and tape volumes of the b^{th}-primitive calculated directly from the design variables.

2.5.5. Minimum tape length constraint

The minimum tape length constraint aims to avoid overly short tapes as shown in Fig. 2d. This constraint emanates from both a numerical and a manufacturing perspective. A short tape brings both end points of mid-axis very close, and that makes the primitive too sensitive to their coordinate variables. At the same time, short tape is also difficult to cut and fabricate on a substrate. With that in consideration, we employ the minimum tape length constraint as,

$$g_l := \frac{1}{fV_0}\sum_{b=1}^{n_b} W_t^b \widetilde{R}\left(L_t^{\min} - L_t^b\right) \leq 0, \tag{19}$$

where $L_t^{\min}$ is the minimum allowed tape length.

2.5.6. Environmental impact constraint

The environmental impact constraint is formulated to quantify the sustainability of the proposed hybrid structures. Various environmental impact metrics have been proposed in the literature [78–80], including global warming potential (GWP), acidification potential (AP), greenhouse gas emissions (GHG), eutrophication potential (EP), ozone depletion potential (ODP), and photochemical ozone creation potential (POCP). In the present work, the environmental performance is assessed using GHG emissions expressed as kg CO_2 equivalent.

A cradle-to-gate Life Cycle Assessment (LCA) framework is adopted, considering the environmental impacts from raw material production to the completion of the manufactured component. The assessment includes the production of raw materials, substrate filament extrusion, tape manufacturing, manufacturing using ATLAM (that includes substrate printing and tape laying), material waste generated during manufacturing, post-processing, and transportation of raw materials. The use, maintenance, recycling, and end-of-life phases were excluded because their impacts are application specific, whereas this study develops a general, application-independent framework.

The total GHG emissions of a candidate structure are evaluated as,

$$I = I_{\text{mat}} + I_{\text{fsmfg}} + I_{\text{mfg}} + I_{\text{waste}} + I_{\text{post}} + I_{\text{trans}}, \tag{20}$$

where the individual terms represent the contributions from raw material production I_{mat}, feedstock (substrate filament & tape) manufacturing I_{fsmfg}, structure manufacturing using ATLAM I_{mfg}, manufacturing waste I_{waste}, post-processing I_{post}, and transportation I_{trans}, respectively.

The material-related contributions can be obtained directly from the eco-cost databases, while the manufacturing-related contributions are estimated using process-specific energy consumption models and converted into CO_2 emissions using the corresponding electricity emission factor. The equations utilized for each contribution is given as,

$$I_{\text{mat}} = m_s\ I_s + m_t\ I_t, \tag{21}$$

$$I_{\text{fsmfg}} = \left(m_s\ \psi_s^{\text{fsmfg}} + m_t\ \psi_t^{\text{fsmfg}}\right)\ I_{\text{elec}}, \tag{22}$$

$$I_{\text{mfg}} = \left(V_s\ \psi_s^{\text{mfg}} + L_t\ \psi_t^{\text{mfg}}\right)\ I_{\text{elec}}, \tag{23}$$

$$I_{\text{waste}} = \eta_s^{\text{waste}}\ m_s\ I_s + \eta_t^{\text{waste}}\ m_t\ I_t, \tag{24}$$

$$I_{\text{post}} = \Psi^{\text{post}}\ I_{\text{elec}}, \tag{25}$$

$$I_{\text{trans}} = \left(\left(1+\eta_s^{\text{waste}}\right)\ m_s + \left(1+\eta_t^{\text{waste}}\right)\ m_t\right)\ I_{\text{trans}}, \tag{26}$$

with

$$m_s = \varrho_s(V_s h - V_t h_t), \quad \text{and} \quad m_t = \varrho_t V_t h_t, \tag{27}$$

where ϱ_s, m_s, and I_s, and ϱ_t, m_t, and I_t denote the density, mass, and embodied GHG emissions per unit mass of the substrate and tape materials, respectively. ψ_s^{fsmfg}, and ψ_t^{fsmfg} denote the mass-specific electricity consumption associated with substrate filament manufacturing and tape manufacturing, respectively; ψ_s^{mfg} denotes the volume-specific electricity consumption for substrate printing; and ψ_t^{mfg} denotes the length-specific electricity consumption for tape laying. Ψ^{post} denotes the total electricity consumption required for post-processing operations, including support removal and specimen finishing. I_{elec} and I_{trans} are the electricity and transportation GHG emission factors, respectively. Furthermore, L_t is the total length of the deposited tape and η_s^{waste} and η_t^{waste} are the fractions of material waste associated with the substrate printing and the tape laying, respectively.

To ensure consistency with the range of values of the other constraints, we linearly scale the GHG of the structure I and formulate the constraint of environmental impact g_e as

$$g_e := \frac{I - I^{\min}}{I^{\max} - I^{\min}} \leq f_e, \tag{28}$$

where f_e is the limit on the constraint; while $I^{\min} = I\big|_{V_s = fV_0,\ V_t = 0}$ and $I^{\max} = I\big|_{V_s = fV_0,\ V_t = fV}$ are the values used for scaling I.

3. Topology optimization results

This section presents the numerical verification of the proposed framework. We solve several standard numerical examples, including the cantilever beam problem, the Messerschmitt - Bölkow - Blohm (MBB) beam problem, the L-bracket problem, the cantilever beam with a hole problem and the bridge problem, to show the effectiveness of the proposed framework. Subsequently, we also report experimental test results of the optimized design of the MBB beam problem to validate the framework.

To solve these numerical examples, the required geometric, loading, meshing and optimization parameters are given in Table 1, while the box limits of the design variables are given in Table 2. We consider PA12 supplied by eSUN Industrial Co. Ltd. (Shenzhen, China) as the substrate material and PA12-CF (with 62% volume fraction of carbon fibers) supplied by Suprem SA (Yverdon-les-Bains, Switzerland) as the tape material. The material properties of both materials are given in Table 3. Unless stated otherwise, we take $h = 12$ mm and $h_t = 0.4$ mm.

The optimization problem is solved using the MMA algorithm [82]. The adjoint method [83] is adopted here to compute the sensitivities. We use the convergence criteria, based on the average relative change in the values of the design variables in the last 10 iterations ($e_z^m < e_z^{\min} = 3 \times 10^{-4}$), based on the average relative change in the value of the objective function in the last 10 iterations ($e_c^m < e_c^{\min} = 3 \times 10^{-4}$), based on the maximum number of iterations ($m > m^{\max} = 300$). The associated errors e_z^m and e_c^m at the m^{th}-iteration are defined as follows,

$$e_z^m = \frac{1}{10}\sum_{k=0}^{9}\left\|\sum_{i=1}^{n_d}\frac{z_i^{m-k} - z_i^{m-k-1}}{\max\left(0,\ z_i^{\max} - z_i^{\min}\right)}\right\|_2, \quad \text{and}$$

$$e_c^m = \frac{1}{10}\sum_{k=0}^{9}\left|\frac{c^{m-k} - c^{m-k-1}}{c^{m-k}}\right|. \tag{29}$$

As our optimization problem involves multiple nonlinear constraints, there is a risk that the design gets stuck in poor local minima as shown in Figure S1a. To reduce the likelihood of such scenarios and corresponding poor designs, we activate the non-overlap constraint and the size variable penalization constraint with a continuation scheme. To do so, we multiply the constraint function by,

$$C_g = \frac{\min\left(\max\left(m - m_g^{\min}, 0\right), m_g^{\max} - m_g^{\min}\right)}{m_g^{\max} - m_g^{\min}}, \tag{30}$$

where m is the current iteration number and $m_g^{\min}$ and $m_g^{\max}$ denote the iteration numbers at which the constraint is activated and becomes fully activated, respectively. Based on preliminary parametric studies, we consider $m_g^{\min} = 50$ and $m_g^{\max} = 100$ for the non-overlap constraint, and $m_g^{\min} = 100$ and $m_g^{\max} = 200$ for the size variable penalization constraint. To ensure that optimization does not stop prematurely before full activation of these constraints, we do not allow optimization to stop before 200 iterations.

3.1. Numerical examples

First, we solve the cantilever beam problem with only five constraints, including the volume fraction constraint g_v, the bounding box constraint g_b, the minimum tape length constraint g_l, the non-overlap constraint g_o and the size variable penalization constraint g_α. In other words, we solve the optimization problem referred in Eq. (2) with $\boldsymbol{g} = [g_v,\ g_b,\ g_o,\ g_\alpha,\ g_l]$. The problem domain and the numerical results, including the optimized design, its deformation field, Von Misses stress distribution, tape density, and substrate density, are presented in Fig. 3a. The von Mises stress distribution is shown solely for qualitative visualization of stress state. The formulation does not account for strength, but considers only structural stiffness. Fig. 3b presents the convergence history of the objective and constraints, including the designs at iterations 0, 10, 50, 100, and 300.

From Fig. 3b, we observe that the initial design that has a high compliance value of $c = 1.06 \times 10^7$ Nm evolves into a stiffer design. Similar to any other TO problem, optimization makes a significant improvement in the objective during the initial stage and reaches a substantially optimized state under the influence of g_v, g_b, and g_l. However, since the non-overlap constraint and the size variable penalization constraint are inactive, the designs until 50^{th}-iteration still possess tape-overlapping and semi-transparent primitives (with intermediate values of α) as shown in the detailed views at iterations 10 & 50. Then, as the non-overlap constraint is activated, the overlapping tapes start to disappear and the value of g_o converges to zero. Similarly, as the effect of the size variable penalization constraint begins at the 100^{th}-iteration, the intermediate values of α are progressively pushed toward values of 0/1, and consequently, optimization eliminates all semitransparent primitives between the 110^{th}-115^{th} iteration. Finally, optimization stops at 300^{th}-iteration as the stopping criterion on the maximum number of iterations is satisfied. We can observe that the final design is substantially stiffer ($c = 1.52$ Nm) with 50% volume ($g_v = 0.50$), negligible overlap ($g_o = 6.95 \times 10^{-5}$), negligible straddling tapes ($g_b = 1.15 \times 10^{-4}$), no short tapes ($g_l = 0$) and no semitransparent primitives ($g_\alpha = 6.99 \times 10^{-10}$).

From Fig. 3 and Table 2, we can observe that the tape width limits were set close to maintain an almost constant width during optimization. This choice is primarily driven by real-world applicability, reflecting tapes with standard widths being utilized in practice.

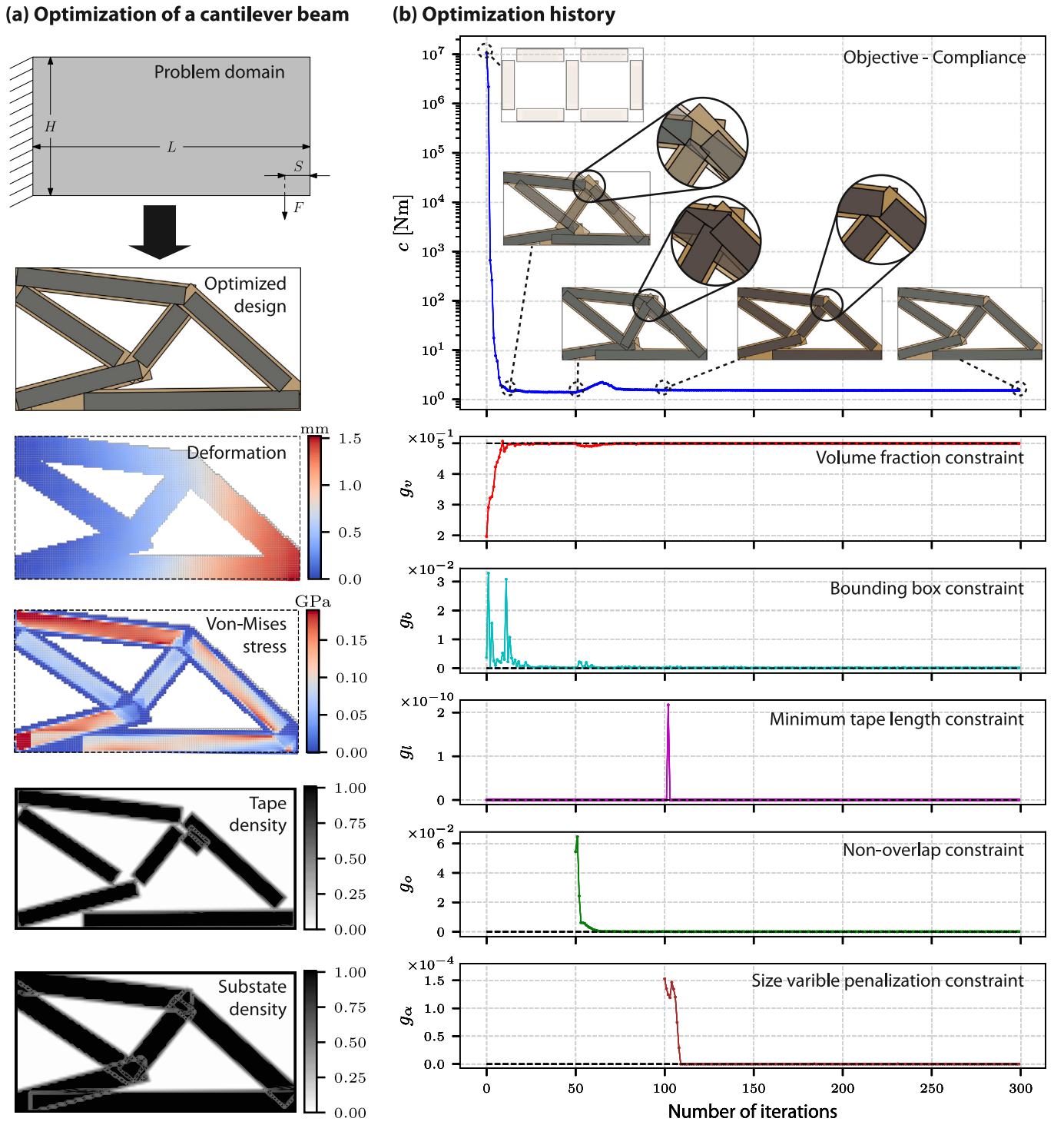


Fig. 3. Topology optimization of a 2D cantilever beam problem using the proposed method - (a) the problem domain, optimized design, deformation field & Von-Mises stress distribution, tape & substrate densities of the optimized design, (b) convergence history of the objective (compliance) and the constraint functions (volume fraction constraint, bounding box constraint, minimum tape length constraint, non-overlap constraint and size variable penalization constraint). It also showcases initial design, final design and the intermediate designs at iteration 10, 50 and 100.

Nonetheless, the TO framework is not restricted by this choice and can still accommodate variable tape widths, as demonstrated in Figure S1a. Figure S1a also highlights the importance of the continuation scheme and the size-variable penalization constraint, as their absence can lead to designs that are infeasible or impractical. Furthermore, we performed a study on the effect of the number of primitives and the volume fraction limit on optimized designs, and the results are given in Figure S1b. As expected, the local minima achieved substantially depend on the initial designs and hyper-parameters.

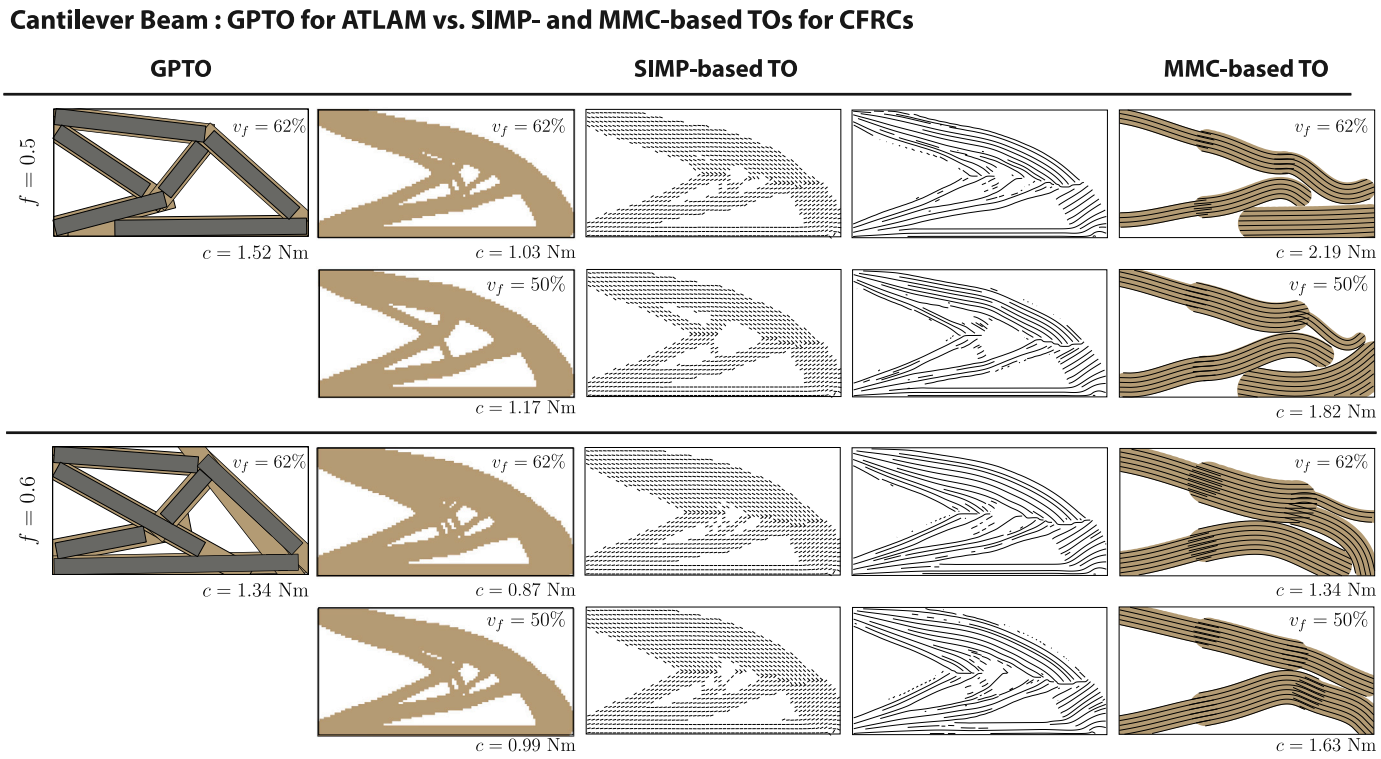


Fig. 4. Comparison of topology-optimized designs for the cantilever beam problem using the proposed GPTO approach for ATLAM, SIMP-based TO [81], and MMC-based TO [72] for CFRCs, including corresponding compliance values. Results are presented for $f = 0.5, 0.6$.

Table 1
Geometric, loading, meshing and optimization parameters for the numerical examples.

Example	L [mm]	H [mm]	W [mm]	L_C [mm]	H_C [mm]	R_C [mm]	S [mm]	W_s [mm]	F [kN]	n_b	n_e	f
Cantilever beam	200	100	–	–	–	–	6.66	–	1	7	7200 (120 × 60)	0.5
MBB beam (Half)	100	50	–	–	–	–	3.57	–	0.5	17	6272 (112 × 56)	0.4
L-bracket	200	200	80	–	–	–	6.66	–	1	29	7200 (120 × 60)	0.5
Cantilever beam with a hole	200	100	–	80	50	30	6.66	–	1	17	7200 (80 × 40)	0.4
Bridge (Half)	300	150	–	–	–	–	7.5	30	1	17	7200 (120 × 60)	0.5

Table 2
Box limits of the design variables associated with the ATLAM primitive.

Example	z_i	x^b_{t1}, x^b_{t2} [mm]	y^b_{t1}, y^b_{t2} [mm]	L^b_{s1}, L^b_{s2} [mm]	W^b_t [mm]	W^b_s [mm]	α^b_t, α^b_s
Cantilever beam, L-bracket, Cantilever beam with a hole, Bridge (Half)	$z_i^{\min}$	0	0	6.35	12.7	17	0
	$z_i^{\max}$	L	H	$\sqrt{L^2+H^2}$	12.7+0.02	21	1
MBB beam (Half)	$z_i^{\min}$	0	0	3.175	6.35	8.5	0
	$z_i^{\max}$	L	H	$\sqrt{L^2+H^2}$	6.35+0.02	11	1

Table 3
Material properties, corresponding values, and sources for the substrate and tape materials.

Material	Property	Symbol	Value	Source
PA12	Young's modulus	E	1.440 GPa	Measured
	Poisson's Ratio	υ	0.403	MatWeb database [84]
	Density	ρ	1.012 $\times 10^3$ kg/m^3	Manufacturer data sheet
PA12-CF	Young's modulus in fiber direction	E_1	133.85 GPa	Measured
	Young's modulus in transverse direction	E_2	3.325 GPa	Calculated
	Poisson's ratio	ν_{12}	0.291	Measured
	Poisson's ratio	ν_{23}	0.420	Calculated
	Shear modulus	G_{12}	1.229 GPa	Calculated
	Density	ρ	1.498 $\times 10^3$ kg/m^3	Manufacturer data sheet
	Fiber volume fraction	v_f	0.62	Manufacturer data sheet

Next, we compare the proposed approach with representative TOs for FRCs from the literature. Specifically, we consider a SIMP-based TO approach using the open-source implementation by Zhao [81], and an MMC-based TO approach with ANCF parameterization following Larsen et al. [72]. As these methods are formulated for fundamentally different numerical problems, they cannot be directly applied in their original form. Therefore, for both approaches, we modify the material model by defining the constitutive matrix as $\mathbb{C}^e = ((h - h_t)\ \mathbb{C}^b_s + h_t\ \mathbb{C}^b_t)$,

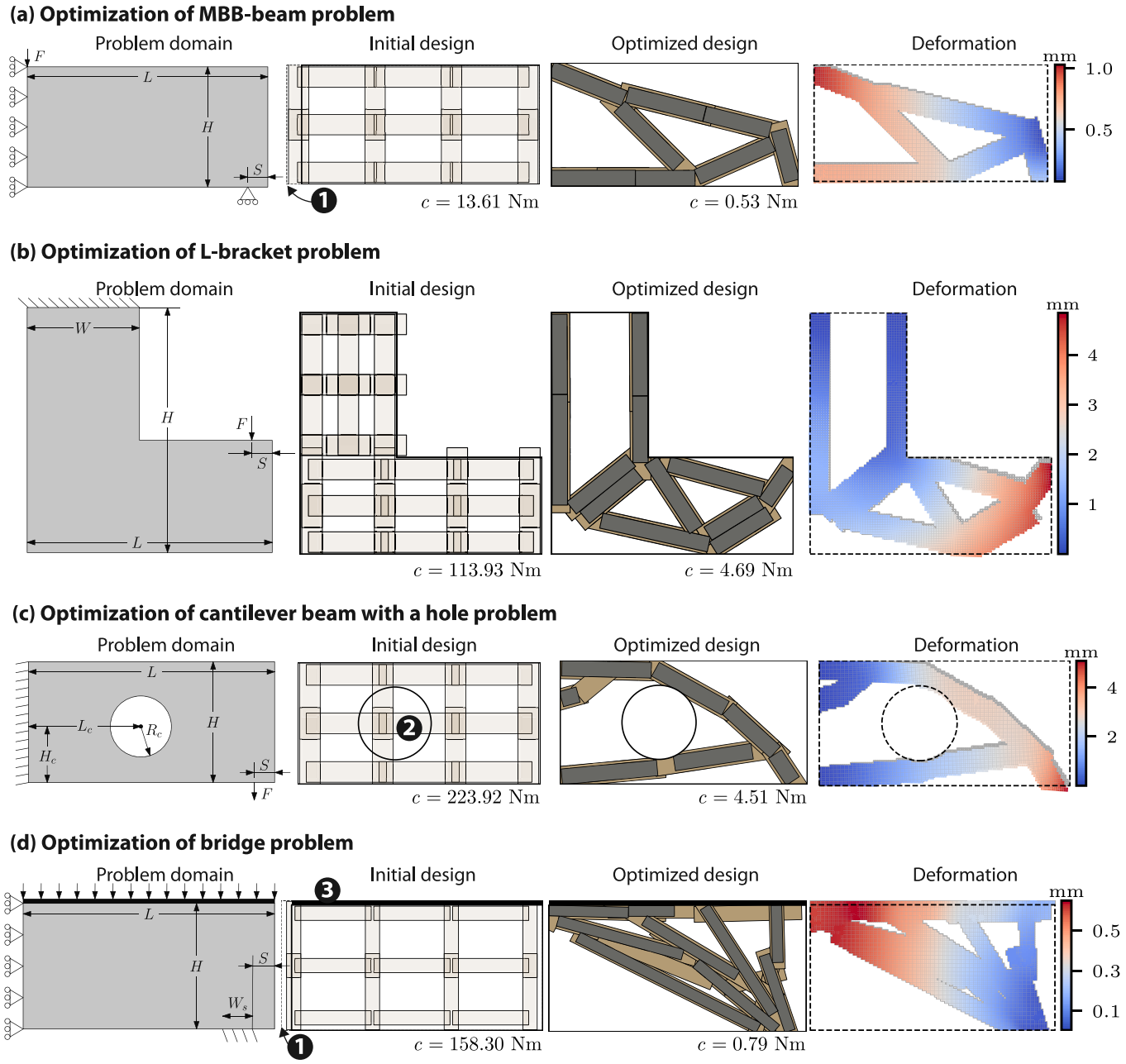


Fig. 5. Topology optimization of (a) MBB beam problem (b) L-bracket problem (c) cantilever beam with a hole problem (d) bridge problem.

to approximate the presence of fiber material only within a layer of thickness h_t, with the remaining region consisting of substrate material.

The results are presented in Fig. 4 for volume fractions $f = 0.5$ and $f = 0.6$. Additional results using an intermediate fiber volume fraction of $v_f = 50\%$ in the reinforced regions for the SIMP- and MMC-based TOs are also presented. This is because the designs generated by SIMP and MMC-based TOs are assumed to be manufactured using CFAM processes, which typically achieve fiber volume fractions of 35%–40% [19], and occasionally up to 50% [20]. Consequently, the effective material properties of the reinforced regions achievable with CFAM are expected to be lower than those attainable with ATLAM.

It can be observed that the GPTO-optimized designs exhibit slightly lower stiffness than the SIMP-optimized designs, even for the case with $v_f = 50\%$. This difference is primarily attributed to the broader design freedom available in the SIMP formulation, which is not subject to the process-specific manufacturing constraints incorporated in the proposed framework. In addition, the fiber orientations obtained from SIMP-based TO are represented as discrete orientation fields and require further post-processing, such as streamline generation or continuous fiber path reconstruction, to obtain manufacturable fiber trajectories. Fig. 4 shows one such reconstruction generated using the evenly-spaced streamline algorithm of Jobard and Lefer [85]. Practical manufacturing considerations, including limitations on fiber curvature, fiber length, feature size, and overlap/gap between fiber paths, may also influence the manufacturability and final structural performance of these designs.

On the other hand, the proposed approach outperforms the MMC-based TO results, despite exhibiting lower fiber path freedom and relatively smaller fiber-covered areas. However, it should be noted that all three approaches address fundamentally different optimization problems and employ distinct design parameterizations. Therefore,

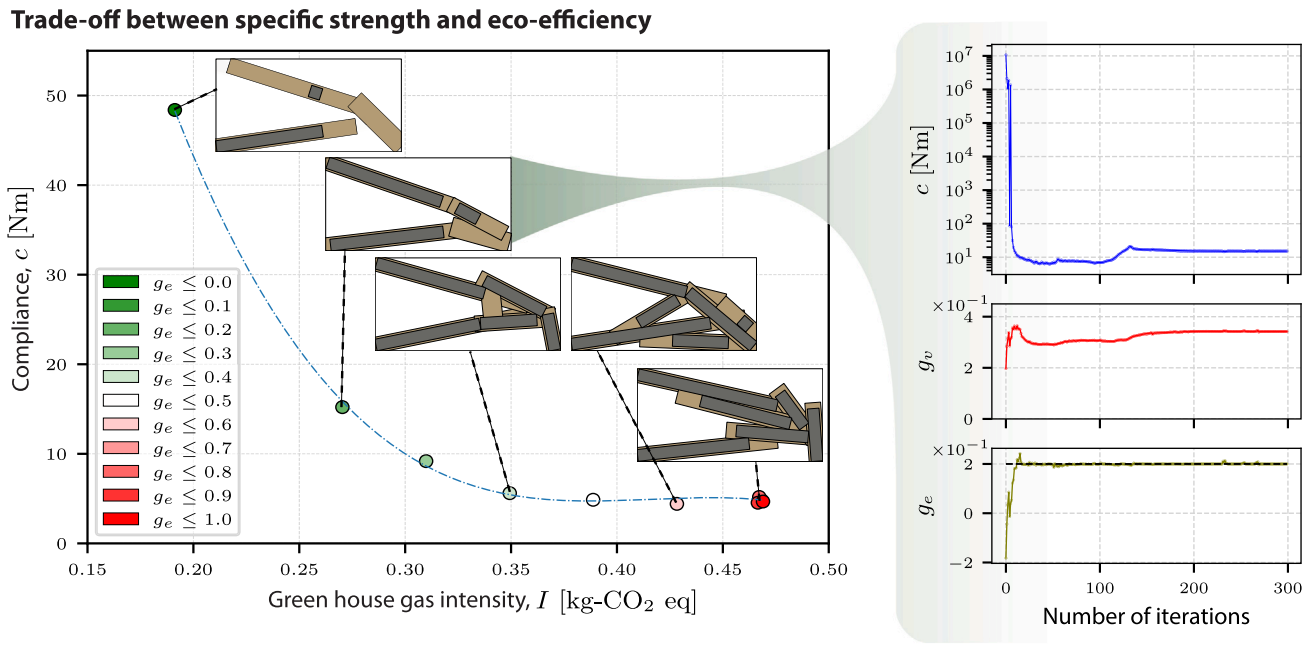


Fig. 6. Trade-off between compliance c (representing stiffness) and green house gas intensity, I (representing environmental impact) with different limits on environmental impact constraint g_e. We also showcase the optimized designs with $g_e \leq 0$, $g_e \leq 0.2$, $g_e \leq 0.4$, $g_e \leq 0.6$, and $g_e \leq 0.8$, and the convergence history of objective, volume fraction constraint and environmental impact constraint for $g_e \leq 0.2$. Other constraint functions are omitted in visualization for brevity.

the obtained results may correspond to different local optima. Nevertheless, the comparative results highlight the effectiveness of the proposed method in achieving competitive stiffness performance while generating manufacturable designs.

Similar to cantilever beam example, we solve the four remaining examples with the same five constraints. The problem domains and the load cases are given in Fig. 5. Note that the MBB-beam and bridge problems exhibit symmetry along the mid-vertical axis. However, if we attempt to solve the problem over the full domain, the results fail to be perfectly symmetric due to numerical tolerances, even when starting from a symmetrical initial design. To avoid this numerical problem, the MBB-beam and bridge case are solved in half domains with symmetry boundary conditions.

The initial designs for the examples are shown in Fig. 5, where the solid black line represents the boundaries of the physical domain, while the dashed black line represents the boundaries of the meshed design domain. We can observe that the design domains are larger than the physical domains for the MBB-beam problem, the cantilever beam with a hole problem, and the bridge problem. The additional portions of the domains are defined as passive zones, which do not influence mechanical behavior but assist in applying several constraints or boundary conditions. All passive zones are annotated in Fig. 3 and explained in Appendix A.

Optimized designs with their compliance values and deformation plots are shown in Fig. 5. The results highlight the robustness of the proposed approach in handling various complex geometric and loading conditions. All optimized designs comply with manufacturing requirements well within the numerical tolerances, while showing improved mechanical performance.

3.1.1. Sustainability aware designs

Next, we showcase the potential of the proposed framework in designing sustainability-aware structures, which can exploit the trade-off capability of the ATLAM process. In order to do so, we also include the environmental impact constraint g_e for the cantilever beam problem, i.e, $\boldsymbol{g} = [g_v,\ g_b,\ g_o,\ g_\alpha,\ g_l,\ g_e]$. Here we take the maximum allowed volume fraction $f = 0.5$, the thickness of structure $h = 2.4$ mm and the total tape reinforcement thickness $h_t = 0.6$ mm to highlight the effect of environmental impact constraint. All other parameters remain as above. The life cycle inventory parameters required to calculate the environmental impact assessment are taken as, I_s=4.610 kg-CO_2 eq/kg, I_t= 64.495 kg-CO_2 eq/kg, $\psi_s^{\text{fsmfg}} = 0.500$ kWh/kg, $\psi_t^{\text{fsmfg}} = 11.0$ kWh/kg, $\psi_s^{\text{mfg}} = 12.0 \times 10^3$ kWh/m^3, $\psi_t^{\text{mfg}} = 0.021$ kWh/m, $\eta_s^{\text{waste}} = 5\%$, $\eta_t^{\text{waste}} = 3\%$, $\Psi^{\text{post}} = 0.0$ kWh, $I_{\text{trans}} = 0.014$ kg-CO_2 eq/kg and $I_{\text{elec}} = 0.244$ kg-CO_2 eq/kWh. The corresponding sources of the parameter values are summarized in Table S1. The results are presented in Fig. 6. It shows a trade-off between compliance and environmental impact for different limits on g_e. The figure also shows the optimized designs for $g_e \leq 0$, $g_e \leq 0.2$, $g_e \leq 0.4$, $g_e \leq 0.6$, and $g_e \leq 0.8$ with the convergence history of compliance c, volume fraction constraint g_v and environmental impact constraint g_e for $g_e \leq 0.2$ (other functions are excluded for the sake of brevity). To highlight the relationship between structural performance and environmental impact, a fitted curve is also included through the optimized solutions. The design corresponding to $g_e \leq 0.1$ was excluded from the curve fitting because the optimization converged to a poor local minimum with a comparatively high compliance ($c = 2.91 \times 10^2$ Nm, $I = 0.22$ kg-CO_2 eq). For the same reason, this point is omitted from the trade-off plot.

From the results, it can be seen that optimized designs use less tape to meet the sustainability criterion for stricter limits on g_e. The choice to satisfy the prescribed sustainability criterion resulted in a corresponding increase in compliance. For the present material system, this behavior arises because the optimizer reduces the amount of PA12-CF tape, which possesses both higher directional stiffness and higher embodied GHG emissions than the PA12 substrate. The optimization convergence history highlights the interplay between objective functions, the volume fraction constraint, and the environmental impact constraint. We can observe that the volume fraction constraint becomes inactive upon using a stringent environmental impact constraint. The sudden increase in c after 100 iterations is attributed to activation of the penalization constraint of the size variable.

4. Experimental validation of topology optimization

It remains to validate the proposed numerical framework in a practical setting. We discuss validation through prototyping and mechanical

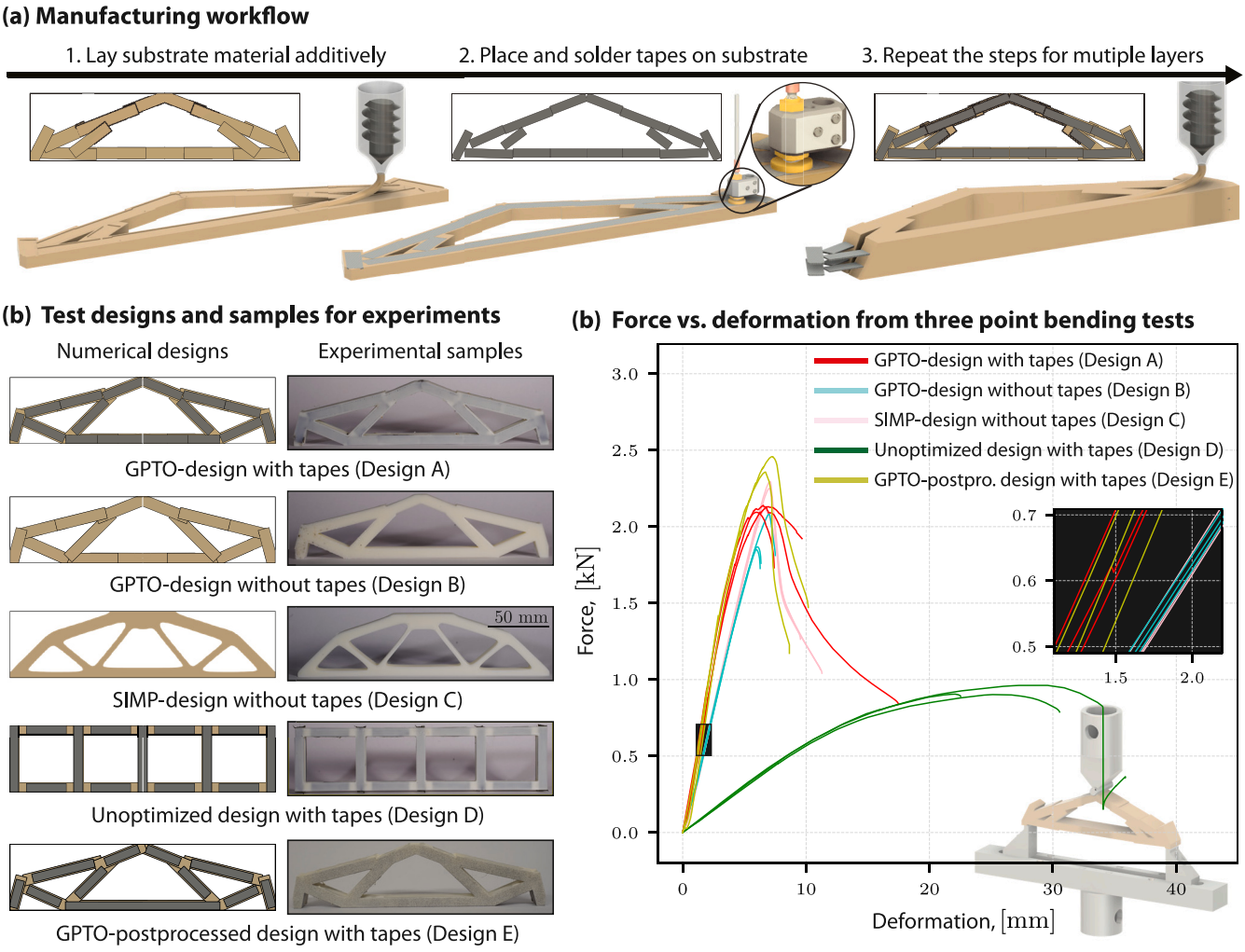


Fig. 7. (a) A small-scale ATLAM workflow using a desktop Fused Deposition Modeling (FDM) 3D-printer, (b) Five test designs with their experimental samples, (c) Force vs. deformation response from three point bending tests.

testing. We chose the optimized design of the MBB beam problem presented in Section 3.1, because it allows mechanical testing through a three-point bending test using a universal testing machine.

4.1. Prototype printing

First, we need to transform the digital design into a physical prototype. We developed a small-scale ATLAM workflow (as shown in Fig. 7a) using a desktop Fused Deposition Modeling (FDM) 3D-printer and an in-house soldering tool-head. We used a PrusaXL multi tool-head printer [86] from Prusa BV., although any desktop polymer 3D-printer would be equally applicable. The in-house tool-head is developed in a way that it can be mounted in place of a PrusaXL tool-head and can utilize the precise automated movement system of the printer.

In this new workflow, we decouple the simultaneous steps of laying the substrate and compressing-bonding the tape of the ATLAM process into two separate steps, as shown in Fig. 7a. In the first step, the substrate is laid additively as in FDM. To execute this step, we need a G-code specifying the print path and process parameters. Therefore, we generate a full 3D CAD model of optimized design using the value of the geometric design variables and a certain thickness. Rectangular tape-thickness slots are embedded in the top surface of this CAD model to predefine the regions for tape placement. Then, the CAD model and other process specifications are fed into the Prusa Slicer software [87] to generate a G-code. By entering this G-code into the printer, we can lay the first layer of substrate material. After the first step, the tapes are placed manually according to the predefined rectangular slots. Next, the heated soldering tool-head is run over the tapes to fusion bond them. We automate the movement of the soldering tool-head using the PrusaXL's movement system to enhance the precision. Then, these steps can be repeated sequentially to generate the entire structure. The thickness of the substrate material in each alternative step can be determined by the number of desired tape layers and their intended placement in the thickness direction.

For the MBB beam design, we use two tape layers, each 0.2 mm thick, placed symmetrically along the thickness direction, with the substrate arranged in three layers of 1.2–9.8–1 mm. The substrate filaments are dried at 70°C in a vacuum oven for 12 h. The process parameters utilized for printing are the following: substrate nozzle temperature 280°C, substrate printing speed 63.6 mm/s, print bed temperature 100°C, soldering tool temperature 280°C, soldering tool speed 150 mm/min.

To enable comparison with our optimized design (hereafter referred to as Design A), we manufacture four additional design samples as: a design identical to GPTO-optimized design but without reinforcement tapes (Design B); a design composed solely of substrate material generated using a SIMP-based density topology optimization approach (Design C) implemented in COMSOL's topology optimization

module; an unoptimized design with tapes (Design D) and a design post-processed from the GPTO-optimized design (Design E). Fig. 7b presents the numerical designs and the experimental samples for all five cases.

4.2. Prototype testing

Next, three-point bending tests are performed on three printed samples for each of the five test designs described in the previous section. For testing, we use a universal testing machine (Zwick 20 kN Universal Test Machine, ZwickRoell, Germany), equipped with a 20 kN load cell. The samples are supported in the testing setup using a fixture with a support span of 192.86 mm and support rollers of 5 mm radii as shown in Figure S2a. The tests are conducted under displacement control at a crosshead speed of 5 mm/min with a preload of 50 N. All tests were performed at room temperature and humidity.

Fig. 7c presents the force–displacement responses measured during the tests. From the force–displacement responses, we calculate the effective bending stiffness (E_{eff}) by linear regression over the linear elastic regime. Using calculated E_{eff}, the elastic strain energy is calculated as $F^2/2E_{\text{eff}}$ at the applied load F. The computed strain energy (at $F = 1$ kN), together with their numerical counterparts, and green house gas intensity I are given in Table 4. Table 4 also presents a measure of the embodied Green House Gas (GHG) per unit of stiffness, strain energy $\times$ I, for all designs.

From the results, we observe that the experimental strain energy values for designs B & D demonstrate very good agreement with the numerical values, within a relative error of 7%–8%. However, there is a substantial discrepancy between both values for design A & D. This discrepancy can be attributed to several possible factors, including the effect of manual intervention for tape laying in the small-scale ATLAM workflow on its precision and accuracy, and the use of a linear rule of mixture. Another aspect is that we use density mapping in topology optimization to define the material distribution for the finite element problem. The accuracy of density mapping depends on mesh resolution, and therefore it cannot capture the small disjoint region between two primitives in close proximity and associated stress concentrations. This effect is corroborated by the comparison of strain ε_{xx}, ε_{yy}, and ε_{xy}, among the results from our in-house code, a full 3D COMSOL simulation performed with a extremely fine mesh consisting 10,821,688 elements, and the experiments, shown in Figure S3b. From the figure, we observe that the strain fields obtained from the in-house finite element model closely match the COMSOL results, while the Digital Image Correlation (DIC) measurements show good qualitative agreement across most of the domain. However, the numerical results do not show any stress concentration in the region of close proximity of two primitives, as in the experimental results. This effect eventually translates into an error in the strain energy estimations. As demonstrated by the COMSOL results, when the gaps are sufficiently large, a finer mesh can capture the disjoint regions more accurately. However, in regions where the tape ends are nearly in contact or slightly overlapping, more advanced FEM approaches capable of tracking discontinuities, localized strain concentrations, and possible separation of contact between adjacent tapes are required. Please note that our results ($c = 0.53$ Nm, $U_{\text{load}} = -1.07$ mm) are in close agreement with the COMSOL results ($c = 0.50$ Nm, $U_{\text{load}} = -1.01$ mm).

To investigate the influence of the close proximity between two primitives, we examine a post-processed design (design E), obtained from the GPTO-optimized design by merging inline primitives and shortening several tapes to avoid close tape-ends. As expected, design E agrees better with the numerical strain energy and shows a higher stiffness with a 14% lower strain energy than design A. This increase in stiffness results from mitigation of stress concentration effects. Despite the improvements, design E exhibits a 30% discrepancy between numerical and experimental results. This discrepancy is consistent with that of design D and underscores the need for improved manufacturing accuracy and the selection of a representative mixture rule.

The Voigt estimate adopted in Eq. (9) assumes perfect strain compatibility and constitutes an upper bound on the effective stiffness. In practice, adhesion between tape and substrate is never perfect, and a finite tangential slip is admissible at each bonding plane, introducing additional compliance that the iso-strain assumption cannot capture. To present a more realistic scenario, we present the strain energy of the investigated designs using a more balanced estimate, the Hill average [88], in Table 4. In our case, Hill average interpolates between the Voigt upper bound and the Reuss lower bound exclusively on the tape increment as,

$$\mathbb{C}^e = \mathbb{C}_{\text{void}} + h \sum_{b=1}^{n_b} \tilde{w}_s^{b,e} \tilde{\rho}_s^{b,e} \left(\mathbb{C}_s^b - \mathbb{C}_{\text{void}}\right) + \gamma\, \Delta\mathbb{C}^e_{\text{tape,V}} + (1-\gamma)\, \Delta\mathbb{C}^e_{\text{tape,R}}, \tag{31}$$

where $\gamma \in [0, 1]$ is a bonding quality parameter, and the Voigt and Reuss tape increments are,

$$\Delta\mathbb{C}^e_{\text{tape,V}} = h_t \sum_{b=1}^{n_b} \tilde{w}_{st}^{b,e} \tilde{\rho}_{st}^{b,e} \left(\mathbb{C}_t^b - \mathbb{C}_s^b\right), \tag{32}$$

$$\Delta\mathbb{C}^e_{\text{tape,R}} = \left[\mathbb{S}_s + h_t \sum_{b=1}^{n_b} \tilde{w}_{st}^{b,e} \tilde{\rho}_{st}^{b,e} \left(\mathbb{S}_t^b - \mathbb{S}_s\right)\right]^{-1} - \mathbb{C}_s, \tag{33}$$

with $\mathbb{S} = \mathbb{C}^{-1}$ denoting the compliance tensor. Here, we take $\gamma = 0.3$. The recalculated strain energies show improved agreement with the experimental results; however, some discrepancies still remain. Therefore, a more detailed investigation of the interface micromechanics, numerical treatment of singularities, and process uncertainties is required to strengthen broader real-world implementation of the proposed method, although these aspects lie beyond the scope of the present work.

Nonetheless, designs A & E outperform other designs in stiffness. Compared to design D, designs A & E are, respectively, 8–9 times and 9–10 times stiffer, highlighting the benefit of optimizing geometry and reinforcement placement using our GPTO method. Design E is 50%–55% stiffer than designs B & C with only substrate material. It exhibits the mechanical advantage of utilizing tape-reinforcement. Intuitively, tape utilization incurs a higher environmental cost. However, when evaluated per unit stiffness, design E with its efficient use of tape achieves stiffness gains greater than the associated sustainability trade-off.

Design A employs tapes over almost the entire design domain, while design B contains no tapes. These designs can be regarded as two extreme cases of tape utilization. Both designs can be manufactured using the ATLAM process based on the focus on stiffness or environmental impact. Additionally, all intermediate designs can be explored with the trading capability of the environmental impact constraint, as explained in Section 3.1.1.

5. Modeling scope and future prospects

The design tool is developed within a GPTO framework to facilitate the treatment of rectangular tapes and the associated manufacturing constraints. The selected manufacturing constraints are chosen based on industrial input provided by CEAD B.V. The geometric primitive, projection scheme, and manufacturing constraints are subsequently formulated in a manner that is both representative of ATLAM process characteristics and compatible with the GPTO framework. To maintain computational tractability, we adopt a two-dimensional structural representation and the Voigt rule-of-mixtures material model that assumes perfect bonding and uniform load transfer between the tape and substrate materials. These assumptions enable an efficient first-order design framework that demonstrates strong predictive capability through the generation of manufacturable designs across multiple design scenarios in the present manuscript. Some discrepancies, however, may

Table 4
Green House Gas (GHG) intensity I, strain energy (numerical & experimental) values, relative error in strain energy and strain energy × I of five test designs considered for three point bending tests.

Test design (Design label)	GHG, I [kg-CO_2 eq]	Strain energy, W_s [J]					$W_s \times I$ [J kg-CO_2 eq]
			Voigt estimate		Hill's average		
	(Num.)	(Exp.)	(Num.)	Error (%)	(Num.)	Error (%)	(Exp.) × (Num.)
GPTO-design with tapes (Design A)	0.503	1.063 ± 0.060	0.538	49.388	0.904	14.957	0.535
GPTO-design without tapes (Design B)	0.382	1.414 ± 0.006	1.452	2.687	1.452	2.687	0.540
SIMP-design without tapes (Design C)	0.353	1.372 ± 0.006	1.281	6.632	1.281	6.632	0.484
Unoptimized design with tapes (Design D)	0.513	8.649 ± 0.099	6.110	29.355	7.467	13.667	4.436
GPTO-postpro. design with tapes (Design E)	0.475	0.913 ± 0.028	0.639	30.011	0.967	5.914	0.433

arise between numerical and experimental results, as certain process-specific effects, including tape–substrate bonding quality, out-of-plane behavior, localized interfacial phenomena, manufacturing tolerances, and process variability, are not yet explicitly accounted for in the model.

Looking ahead, addressing these aspects presents a natural avenue for further enhancing the overall fidelity of the model. The modular nature of the framework allows individual components to be readily extended. In particular, incorporating full three-dimensional simulations alongside improved homogenization schemes and interface-aware constitutive models would enable a more accurate representation of real components. In addition, our structures were designed according to the intended ATLAM process, while our in-house manufacturing workflow employed manual tape placement and soldering-based tape bonding as a surrogate for automated tape laying. This validation could, however, be extended in future to the actual ATLAM process employing automated tape laying, thereby reducing manufacturing errors and further closing the gap between numerical predictions and experimental observations.

6. Conclusions

To exploit the full potential of Advanced Tape Laying Additive Manufacturing (ATLAM), we developed a computational design tool rooted in the Geometric Projection Topology Optimization (GPTO) framework and incorporated various ATLAM-specific constraints. This design tool provides unique ability to balance stiffness, manufacturing flexibility and eco-efficiency. Introducing tape laying into the additive manufacturing process allows for using high performance materials efficiently into structural designs We verified the robustness of the proposed framework by solving five numerical examples: a cantilever beam problem, an MBB beam problem, an L-bracket problem, a cantilever beam with a hole problem and a bridge problem. Our results demonstrate that the proposed method could effectively design substantially stiffer structures with optimized geometry and tailored reinforcement positioning. In addition our method ensures fabrication of the optimized structures by introducing manufacturing constraints such as avoiding tape-overlap, straddling tapes, and short tapes. The proposed method achieves competitive stiffness performance compared to existing TO approaches for continuous FRCs.

Our lab-scale experimental results validate the superior performance of our optimized design compared to other designs. The results also highlight the substantial increase in stiffness by optimizing the geometry and reinforcement placement. Through efficient use of tapes, optimized designs achieve stiffness gains greater than the associated sustainability trade-off. We showcased agreement between numerical and experimental results using Hill's average constitutive relations.

Overall we demonstrate that combining tape laying and additive manufacturing with our design method can realize sustainability-aware manufacturable FRC structures. Accordingly, for a given load case and boundary conditions, a range of ATLAM-manufacturable designs can be generated based on varying stiffness and sustainability requirements, which will become crucial in the development of future sustainable structures.

CRediT authorship contribution statement

Chintan Jansari: Writing – review & editing, Writing – original draft, Visualization, Validation, Software, Resources, Project administration, Methodology, Investigation, Formal analysis, Data curation, Conceptualization. **David Canosa Ybarra:** Validation, Investigation. **Matthijs Langelaar:** Writing – review & editing, Supervision, Resources, Conceptualization. **Can Ayas:** Writing – review & editing, Supervision, Resources, Conceptualization. **Kunal Masania:** Writing – review & editing, Supervision, Resources, Project administration, Funding acquisition, Conceptualization.

Declaration of competing interest

The authors declare that they have no known competing financial interests or personal relationships that could have appeared to influence the work reported in this paper.

Acknowledgments

We acknowledge funding from the National Growth Fund Program NXTGEN HIGHTECH.

Appendix A. Passive zones

We define the passive zone as the portion of the design domain that does not belong to the physical domain, and eases applying a particular constraint or boundary condition. We utilize three types of passive zones as given in Table A.5.

The first type is utilized to ensure the proper application of the bounding box constraint along the boundaries where symmetric boundary conditions are applied. The bounding box constraint restricts the tape to cross the boundary with symmetry conditions, even though there is no manufacturability requirement for it. Also, as the bounding box constraint is designed based on volume difference, it is not straightforward to deactivate it along these boundaries. Therefore, we consider a slightly larger design domain than the actual physical domain in the direction of the symmetry boundary conditions, as illustrated in Fig. 5a & Fig. 5d. In order to ensure that the passive zone does not affect the mechanical problem and the volume fraction constraint, we set the densities $\tilde{\rho}_s^{be}$ and $\tilde{\rho}_s^{be}$ to zero within the zone. Note that ρ_t^{be}-values are still non-zero, so V_t in the bounding box constraint will account for the tape-volume inside the zone.

The second type is utilized to introduce a hole in the design domain. Alternatively, a mesh conforming to the hole boundary could be created. However, we utilize this passive zone to make use of a uniform structured mesh. The third type is similar to the second; the only difference is that this zone is filled with substrate material. It works as an extra substrate material that remains unchanged during optimization and, therefore, the distributed load on its boundary also remains unchanged.

Table A.5
Objectives and numerical conditions for different type of passive zone used in the numerical examples.

Type	Objective	Conditions
1	To inactivate bounding box constraint along boundaries with symmetric boundary conditions	$\bar{\rho}_s^{b,e} = 0,\ \bar{\rho}_s^{b,e} = 0$
2	To introduce a hole	$\bar{\rho}_s^{b,e} = 0,\ \bar{\rho}_t^{b,e} = 0,$ $\bar{\rho}_s^{b,e} = 0,\ \bar{\rho}_t^{b,e} = 0$
3	To preserve the boundary for applying the distributed load	$\bar{\rho}_s^{b,e} = 1,\ \bar{\rho}_t^{b,e} = 0,$ $\bar{\rho}_s^{b,e} = 1,\ \bar{\rho}_t^{b,e} = 0$

Appendix B. Supplementary data

Supplementary material related to this article can be found online at https://doi.org/10.1016/j.addma.2026.105320.

Data availability

Data will be made available on request.

References

[1] P.K. Mallick, Fiber-reinforced Composites: Materials, Manufacturing, and Design, CRC Press, 2007.
[2] C.E. Harris, J.H. Starnes Jr., M.J. Shuart, Design and manufacturing of aerospace composite structures, state-of-the-art assessment, J. Aircr. 39 (4) (2002) 545–560.
[3] C. Soutis, Carbon fiber reinforced plastics in aircraft construction, Mater. Sci. Eng.: A 412 (1) (2005) 171–176, http://dx.doi.org/10.1016/j.msea.2005.08.064, International Conference on Recent Advances in Composite Materials.
[4] P. Beardmore, Composite structures for automobiles, Compos. Struct. 5 (3) (1986) 163–176.
[5] G. Savage, Composite materials in formula 1 racing, Met. Mater. Bury St Edmunds 7 (10) (1991) 617–624.
[6] L. Hollaway, The evolution of and the way forward for advanced polymer composites in the civil infrastructure, Constr. Build. Mater. 17 (6–7) (2003) 365–378, http://dx.doi.org/10.1016/S0950-0618(03)00038-2.
[7] V.M. Karbhari, Fiber reinforced composite bridge systems - transition from the laboratory to the field, Compos. Struct. 66 (1–4) (2004) 5–16, http://dx.doi.org/10.1016/j.compstruct.2004.04.026.
[8] A. Brasington, C. Sacco, J. Halbritter, R. Wehbe, R. Harik, Automated fiber placement: a review of history, current technologies, and future paths forward, Compos. Part C: Open Access 6 (2021) 100182.
[9] K. Yassin, M. Hojjati, Processing of thermoplastic matrix composites through automated fiber placement and tape laying methods: A review, J. Thermoplast. Compos. Mater. 31 (12) (2018) 1676–1725.
[10] S. Ashley, Rapid prototyping systems, Mech. Eng. 113 (1991) 34–43.
[11] T.D. Ngo, A. Kashani, G. Imbalzano, K.T. Nguyen, D. Hui, Additive manufacturing (3D printing): A review of materials, methods, applications and challenges, Compos. Part B: Eng. 143 (2018) 172–196, http://dx.doi.org/10.1016/j.compositesb.2018.02.012.
[12] O. Abdulhameed, A. Al-Ahmari, W. Ameen, S.H. Mian, Additive manufacturing: Challenges, trends, and applications, Adv. Mech. Eng. 11 (2) (2019) 1687814018822880.
[13] W. Zhong, F. Li, Z. Zhang, L. Song, Z. Li, Short fiber reinforced composites for fused deposition modeling, Mater. Sci. Eng.: A 301 (2) (2001) 125–130, http://dx.doi.org/10.1016/S0921-5093(00)01810-4.
[14] O. Carneiro, A. Silva, R. Gomes, Fused deposition modeling with polypropylene, Mater. Des. 83 (2015) 768–776, http://dx.doi.org/10.1016/j.matdes.2015.06.053.
[15] F. Ning, W. Cong, J. Qiu, J. Wei, S. Wang, Additive manufacturing of carbon fiber reinforced thermoplastic composites using fused deposition modeling, Compos. Part B: Eng. 80 (2015) 369–378, http://dx.doi.org/10.1016/j.compositesb.2015.06.013.
[16] R. Matsuzaki, M. Ueda, M. Namiki, T.-K. Jeong, H. Asahara, K. Horiguchi, T. Nakamura, A. Todoroki, Y. Hirano, Three-dimensional printing of continuous-fiber composites by in-nozzle impregnation, Sci. Rep. 6 (1) (2016) 23058, http://dx.doi.org/10.1038/srep23058.
[17] X. Tian, T. Liu, C. Yang, Q. Wang, D. Li, Interface and performance of 3D printed continuous carbon fiber reinforced PLA composites, Compos. Part A: Appl. Sci. Manuf. 88 (2016) 198–205, http://dx.doi.org/10.1016/j.compositesa.2016.05.032.
[18] G.W. Melenka, B.K. Cheung, J.S. Schofield, M.R. Dawson, J.P. Carey, Evaluation and prediction of the tensile properties of continuous fiber-reinforced 3D printed structures, Compos. Struct. 153 (2016) 866–875, http://dx.doi.org/10.1016/j.compstruct.2016.07.018.
[19] G.D. Goh, Y.L. Yap, S. Agarwala, W.Y. Yeong, Recent progress in additive manufacturing of fiber reinforced polymer composite, Adv. Mater. Technol. 4 (1) (2019) 1800271, http://dx.doi.org/10.1002/admt.201800271.
[20] T. Liu, X. Tian, Y. Zhang, Y. Cao, D. Li, High-pressure interfacial impregnation by micro-screw in-situ extrusion for 3D printed continuous carbon fiber reinforced nylon composites, Compos. Part A: Appl. Sci. Manuf. 130 (2020) 105770, http://dx.doi.org/10.1016/j.compositesa.2020.105770.
[21] CEAD B.V., CEAD B.V., Delft, Netherlands, 2014, URL https://ceadgroup.com/.
[22] G. Gardiner, ATLAM combines composite tape laying, large-scale thermoplastic 3D printing in one printhead, CompositesWorld (2023) URL https://www.compositesworld.com/news/atlam-combines-composite-tape-laying-large-scale-thermoplastic-3d-printing-in-one-printhead.
[23] C. Poli, Design for Manufacturing: a Structured Approach, Butterworth-Heinemann, Boston, 2001.
[24] M.K. Thompson, G. Moroni, T. Vaneker, G. Fadel, R.I. Campbell, I. Gibson, A. Bernard, J. Schulz, P. Graf, B. Ahuja, F. Martina, Design for additive manufacturing: Trends, opportunities, considerations, and constraints, CIRP Ann 65 (2) (2016) 737–760, http://dx.doi.org/10.1016/j.cirp.2016.05.004.
[25] J. Wong, A. Altassan, D.W. Rosen, Additive manufacturing of fiber-reinforced polymer composites: A technical review and status of design methodologies, Compos. Part B: Eng. 255 (2023) 110603, http://dx.doi.org/10.1016/j.compositesb.2023.110603.
[26] D. Moreno Nieto, D. Moreno Sánchez, Design for additive manufacturing: Tool review and a case study, Appl. Sci. 11 (4) (2021) 1571, http://dx.doi.org/10.3390/app11041571.
[27] M.P. Bendsøe, Optimal shape design as a material distribution problem, Struct. Optim. 1 (4) (1989) 193–202, http://dx.doi.org/10.1007/BF01650949.
[28] M.P. Bendsøe, O. Sigmund, Material interpolation schemes in topology optimization, Arch. Appl. Mech. (Ingenieur Archiv) 69 (9–10) (1999) 635–654, http://dx.doi.org/10.1007/s004190050248.
[29] M.Y. Wang, X. Wang, D. Guo, A level set method for structural topology optimization, Comput. Methods Appl. Mech. Engrg. 192 (1–2) (2003) 227–246.
[30] F. Wein, P.D. Dunning, J.A. Norato, A review on feature-mapping methods for structural optimization, Struct. Multidiscip. Optim. 62 (4) (2020) 1597–1638, http://dx.doi.org/10.1007/s00158-020-02649-6.
[31] Z. Li, H. Xu, S. Zhang, A comprehensive review of explicit topology optimization based on moving morphable components (MMC) method, Arch. Comput. Methods Eng. (2024) http://dx.doi.org/10.1007/s11831-023-10053-8.
[32] Y. Mei, X. Wang, G. Cheng, A feature-based topological optimization for structure design, Adv. Eng. Softw. 39 (2) (2008) 71–87, http://dx.doi.org/10.1016/j.advengsoft.2007.01.023.
[33] S. Lee, B.M. Kwak, Smooth boundary topology optimization for eigenvalue performance and its application to the design of a flexural stage, Eng. Optim. 40 (3) (2008) 271–285, http://dx.doi.org/10.1080/03052150701693198.
[34] A. Saxena, Are circular shaped masks adequate in adaptive mask overlay topology synthesis method? J. Mech. Des. 133 (011001) (2010) http://dx.doi.org/10.1115/1.4002973.
[35] X. Guo, W. Zhang, W. Zhong, Doing topology optimization explicitly and geometrically—A new moving morphable components based framework, J. Appl. Mech. 81 (081009) (2014) http://dx.doi.org/10.1115/1.4027609.
[36] J. Norato, B. Bell, D. Tortorelli, A geometry projection method for continuum-based topology optimization with discrete elements, Comput. Methods Appl. Mech. Engrg. 293 (2015) 306–327, http://dx.doi.org/10.1016/j.cma.2015.05.005.
[37] W. Zhang, J. Chen, X. Zhu, J. Zhou, D. Xue, X. Lei, X. Guo, Explicit three dimensional topology optimization via Moving Morphable Void (MMV) approach, Comput. Methods Appl. Mech. Engrg. 322 (2017) 590–614, http://dx.doi.org/10.1016/j.cma.2017.05.002.
[38] V.-N. Hoang, G.-W. Jang, Topology optimization using moving morphable bars for versatile thickness control, Comput. Methods Appl. Mech. Engrg. 317 (2017) 153–173, http://dx.doi.org/10.1016/j.cma.2016.12.004.
[39] X. Zhang, G. Sun, C. Wang, H. Li, S. Zhou, A review of structural topology optimization for fiber-reinforced composites, Compos. Part B: Eng. 299 (2025) 112393, http://dx.doi.org/10.1016/j.compositesb.2025.112393.
[40] J. Stegmann, E. Lund, Discrete material optimization of general composite shell structures, Internat. J. Numer. Methods Engrg. 62 (14) (2005) 2009–2027, http://dx.doi.org/10.1002/nme.1259.
[41] S. Setoodeh, M. Abdalla, Z. Gürdal, Design of variable-stiffness composite panels for maximum buckling load, Compos. Struct. 87 (1) (2009) 109–117, http://dx.doi.org/10.1016/j.compstruct.2008.01.022.
[42] T. Nomura, E. Dede, T. Matsumori, A. Kawamoto, Simultaneous optimization of topology and orientation of anisotropic material using a level set method, Struct. Multidiscip. Optim. 40 (1–6) (2010) 519–531, http://dx.doi.org/10.1007/s00158-010-0502-4.
[43] A. Malakhov, A. Polilov, Design of composite structures reinforced curvilinear fibres using FEM, Compos. Part A: Appl. Sci. Manuf. 87 (2016) 23–28, http://dx.doi.org/10.1016/j.compositesa.2016.04.012.

[44] K. Sugiyama, R. Matsuzaki, A.V. Malakhov, A.N. Polilov, M. Ueda, A. Todoroki, et al., 3D printing of optimized composites with variable fiber volume fraction and stiffness using continuous fiber, Compos. Sci. Technol. 186 (2020) 107905, http://dx.doi.org/10.1016/j.compscitech.2019.107905.

[45] M.A. Nik, K. Fayazbakhsh, D. Pasini, L. Lessard, Surrogate-based multi-objective optimization of a composite laminate with curvilinear fibers, Compos. Struct. 94 (8) (2012) 2306–2313, http://dx.doi.org/10.1016/j.compstruct.2012.03.017.

[46] J. Zhang, W.-H. Zhang, J.-H. Zhu, An extended stress-based method for orientation angle optimization of composite structures, Struct. Multidiscip. Optim. (2013).

[47] H. Li, L. Gao, H. Li, X. Li, H. Tong, Full-scale topology optimization for fiber-reinforced structures with continuous fiber paths, Comput. Methods Appl. Mech. Engrg. 377 (2021) 113668, http://dx.doi.org/10.1016/j.cma.2021.113668.

[48] Y. Xu, Y. Gao, C. Wu, J. Fang, G. Sun, Concurrent optimization of topological configuration and continuous fiber path for composite structures: A unified level-set framework, Struct. Multidiscip. Optim. 65 (214) (2022) http://dx.doi.org/10.1007/s00158-022-03266-2.

[49] S. Jung, D. Kim, G.H. Yoon, Multiscale topology optimization of fiber-reinforced composites considering local fiber size and orientation design, Compos. Struct. 295 (2022) 115824, http://dx.doi.org/10.1016/j.compstruct.2022.115824.

[50] F.S. Almeida Jr., I.B.C.M. Rocha, E.C.N. Silva, Concurrent topology and fiber orientation optimization of additively manufactured composite structures, Addit. Manuf. 72 (2023) 103563, http://dx.doi.org/10.1016/j.addma.2023.103563.

[51] M. Huang, Q. Zhao, P. Li, Progressive concurrent topology optimization of composite structures considering fiber orientation and fiber content, Compos. Struct. 320 (2023) 117208, http://dx.doi.org/10.1016/j.compstruct.2023.117208.

[52] M. Mokhtarzadeh, R. Tavakoli, S. Mohammadi, Concurrent level-set and fiber orientation optimization of composite structures with manufacturability constraints, Struct. Multidiscip. Optim. 67 (2024) 98, http://dx.doi.org/10.1007/s00158-024-03782-1.

[53] T. Luo, X. Chen, J. Wang, Buckling-constrained topology optimization of manufacturable continuous fiber composite structures, Compos. Struct. 334 (2024) 117945, http://dx.doi.org/10.1016/j.compstruct.2024.117945.

[54] Q. Li, R. Sun, K. Zhang, Strength-based collaborative topology optimization for fiber-reinforced composite structures under failure constraints, Compos. Part B: Eng. 286 (2024) 111728, http://dx.doi.org/10.1016/j.compositesb.2024.111728.

[55] Y. Cheng, L. Xu, T. Gao, Isogeometric topology optimization of fiber reinforced composite structures considering stress constraints and load uncertainties, Comput. Methods Appl. Mech. Engrg. 435 (2025) 117512, http://dx.doi.org/10.1016/j.cma.2025.117512.

[56] A. Chandrasekhar, P. Kumar, G.H. Paulino, FRC-TOuNN: Topology optimization of continuous fiber reinforced composites using neural networks, Comput. Methods Appl. Mech. Engrg. 412 (2023) 116061, http://dx.doi.org/10.1016/j.cma.2023.116061.

[57] T. Liu, T. Zhang, Y. Chen, W. Wang, Y. Jiang, Y. Huang, C.C.L. Wang, Neural co-optimization of structural topology, manufacturable layers, and path orientations for fiber-reinforced composites, 2025, arXiv preprint arXiv:2505.03779, arXiv:2505.03779.

[58] R.R. Fernandes, N. van de Werken, P. Koirala, T. Yap, A.Y. Tamijani, M. Tehrani, Experimental investigation of additively manufactured continuous fiber reinforced composite parts with optimized topology and fiber paths, Addit. Manuf. 44 (2021) 102056, http://dx.doi.org/10.1016/j.addma.2021.102056.

[59] Y. Gandhi, G. Minak, A review on topology optimization strategies for additively manufactured continuous fiber-reinforced composite structures, Appl. Sci. 12 (21) (2022) http://dx.doi.org/10.3390/app122111211.

[60] B. Szederkenyi, N.K. Kovacs, T. Czigany, A comprehensive review of fiber-reinforced topology optimization for advanced polymer composites produced by automated manufacturing, Adv. Ind. Eng. Polym. Res. 8 (1) (2025) 113–131, http://dx.doi.org/10.1016/j.aiepr.2024.05.002.

[61] Z. Qian, G.K. Ananthasuresh, Optimal embedding of rigid objects in the topology design of structures, Mech. Based Des. Struct. Mach. 32 (2) (2004) 165–193, http://dx.doi.org/10.1081/SME-120030555.

[62] J. Zhu, W. Zhang, P. Beckers, Integrated layout design of multi-component system, Internat. J. Numer. Methods Engrg. 78 (6) (2009) 631–651, http://dx.doi.org/10.1002/nme.2499.

[63] Z. Kang, Y. Wang, Integrated topology optimization with embedded movable holes based on combined description by material density and level sets, Comput. Methods Appl. Mech. Engrg. 255 (2013) 1–13, http://dx.doi.org/10.1016/j.cma.2012.11.006.

[64] J.-H. Zhu, H.-H. Gao, W.-H. Zhang, Y. Zhou, A Multi-point constraints based integrated layout and topology optimization design of multi-component systems, Struct. Multidiscip. Optim. 51 (2) (2015) 397–407, http://dx.doi.org/10.1007/s00158-014-1134-7.

[65] Y. Wang, Z. Luo, X. Zhang, Z. Kang, Topological design of compliant smart structures with embedded movable actuators, Smart Mater. Struct. 23 (4) (2014) 045024, http://dx.doi.org/10.1088/0964-1726/23/4/045024.

[66] W. Zhang, Y. Zhou, J. Zhu, A comprehensive study of feature definitions with solids and voids for topology optimization, Comput. Methods Appl. Mech. Engrg. 325 (2017) 289–313, http://dx.doi.org/10.1016/j.cma.2017.07.004.

[67] W. Zhang, J. Song, J. Zhou, Z. Du, Y. Zhu, Z. Sun, X. Guo, Topology optimization with multiple materials via moving morphable component (MMC) method, Internat. J. Numer. Methods Engrg. 113 (11) (2018) 1653–1675, http://dx.doi.org/10.1002/nme.5714.

[68] Z. Sun, Z. Song, J. Song, H. Li, Structural optimization of fiber-reinforced material based on Moving Morphable Components (MMCs), Acta Mech. Solida Sin. 35 (4) (2022) 632–646, http://dx.doi.org/10.1007/s10338-021-00305-0.

[69] V.-N. Hoang, N.-L. Nguyen, H. Nguyen-Xuan, Topology optimization of coated structure using moving morphable sandwich bars, Struct. Multidiscip. Optim. 61 (2) (2020) 491–506, http://dx.doi.org/10.1007/s00158-019-02370-z.

[70] B.V. De Almeida, R. Pavanello, M. Langelaar, Topology optimization of smart structures with embedded piezoelectric stack actuators using a composite geometry projection method, Comput. Methods Appl. Mech. Engrg. 429 (2024) 117120, http://dx.doi.org/10.1016/j.cma.2024.117120.

[71] Y. Gandhi, A.M. Aragón, J. Norato, G. Minak, A geometry projection method for the topology optimization of additively manufactured variable-stiffness composite laminates, Comput. Methods Appl. Mech. Engrg. 435 (2025) 117663, http://dx.doi.org/10.1016/j.cma.2024.117663.

[72] A.W.W. Larsen, F.B.H. Østergaard, E. Lund, Component-based 2D topology and continuous fiber layout optimization of additively manufactured parts, Struct. Multidiscip. Optim. 69 (3) (2026) 63, http://dx.doi.org/10.1007/s00158-025-04223-4.

[73] J. Norato, R. Haber, D. Tortorelli, M. Bendsøe, A geometry projection method for shape optimization, International J. Numer. Methods Eng. 60 (14) (2004) 2289–2312.

[74] H. Smith, J.A. Norato, Topology optimization with discrete geometric components made of composite materials, Comput. Methods Appl. Mech. Engrg. 376 (2021) 113582, http://dx.doi.org/10.1016/j.cma.2020.113582.

[75] H. Smith, J. Norato, Topology optimization of structures made of fiber-reinforced plates, Struct. Multidiscip. Optim. 65 (2) (2022) 58, http://dx.doi.org/10.1007/s00158-021-03164-y.

[76] H. Smith, J. Norato, Simultaneous material and topology optimization of composite laminates, Comput. Methods Appl. Mech. Engrg. 404 (2023) 115781, http://dx.doi.org/10.1016/j.cma.2022.115781.

[77] S. Zhang, J.A. Norato, Optimal design of panel reinforcements with ribs made of plates, J. Mech. Des. 139 (081403) (2017) http://dx.doi.org/10.1115/1.4036999.

[78] J. Bare, TRACI 2.0: the tool for the reduction and assessment of chemical and other environmental impacts 2.0, Clean Technol. Environ. Policy 13 (5) (2011) 687–696, http://dx.doi.org/10.1007/s10098-010-0338-9.

[79] J.C. Salcido, A.A. Raheem, S. Ravi, Comparison of embodied energy and environmental impact of alternative materials used in reticulated dome construction, Build. Environ. 96 (2016) 22–34, http://dx.doi.org/10.1016/j.buildenv.2015.11.010.

[80] R.D. Kundu, X.S. Zhang, Sustainability-oriented multimaterial topology optimization: designing efficient structures incorporating environmental effects, Struct. Multidiscip. Optim. 68 (1) (2025) 1–20, http://dx.doi.org/10.1007/s00158-024-03930-8.

[81] J. Zhao, CFRCTop: An Efficient MATLAB implementation for topology optimization of continuous fiber-reinforced composite structures, Appl. Sci. 15 (17) (2025) 9242, http://dx.doi.org/10.3390/app15179242.

[82] K. Svanberg, The method of moving asymptotes—a new method for structural optimization, Internat. J. Numer. Methods Engrg. 24 (2) (1987) 359–373, http://dx.doi.org/10.1002/nme.1620240207.

[83] J.S. Arora, E.J. Haug, Methods of design sensitivity analysis in structural optimization, AIAA J. 17 (9) (1979) 970–974, http://dx.doi.org/10.2514/3.61260.

[84] L. MatWeb, MatWeb material property data, 2026, https://www.matweb.com/.

[85] B. Jobard, W. Lefer, Creating evenly-spaced streamlines of arbitrary density, in: W. Lefer, M. Grave (Eds.), Visualization in Scientific Computing '97, Springer Vienna, Vienna, 1997, pp. 43–55.

[86] Prusa Research s.r.o., Original Prusa XL 3D printer, 2024, Core-XY, up to 5 tool-heads, build volume 360 ×360 ×360 mm, https://www.prusa3d.com/en/product/original-prusa-xl-assembled-5-toolhead-3d-printer/.

[87] Prusa Research s.r.o., PrusaSlicer, 3D Printing Software, 2023, https://www.prusa3d.com/prusaslicer/.

[88] R. Hill, The elastic behaviour of a crystalline aggregate, Proc. Phys. Soc. A 65 (5) (1952) 349–354, http://dx.doi.org/10.1088/0370-1298/65/5/307.